Journal of Alloys and Compounds 686 (2016) 453–466

Contents lists available at ScienceDirect

Journal of Alloys and Compounds

journal homepage: http://www.elsevier.com/locate/jalcom

Optical and magnetic nanocomposites containing Fe_3O_4@SiO_2 grafted with Eu^{3+} and Tb^{3+} complexes

L.U. Khan [a], D. Muraca [b], H.F. Brito [a, *], O. Moscoso-Londoño [b], M.C.F.C. Felinto [c], K.R. Pirota [b], E.E.S. Teotonio [d], O.L. Malta [e]

[a] Department of Fundamental Chemistry, Institute of Chemistry, University of Sao Paulo, Av. Prof. Lineu Prestes, 748, 05508-000 São Paulo, SP, Brazil
[b] Institute of Physics "Gleb Wataghin", Condensed Matter Physics Department, State University of Campinas (UNICAMP), 13083-859 Campinas, SP, Brazil
[c] Nuclear and Energy Research Institute (IPEN-CQMA), Av. Prof. Lineu Prestes, 2242, 05508-000 São Paulo, SP, Brazil
[d] Department of Chemistry, Federal University of Paraiba, 58051-970 João Pessoa, PB, Brazil
[e] Department of Fundamental Chemistry, Federal University of Pernambuco, 50670-901 Recife, PE, Brazil

ARTICLE INFO

Article history:
Received 4 March 2016
Received in revised form
14 May 2016
Accepted 3 June 2016
Available online 7 June 2016

Keywords:
Europium
Terbium
Magnetite
Silica
Photoluminescence and magnetism

ABSTRACT

The fabrication of bifunctional nanocomposites, co-assembling photonic (RE^{3+}) and magnetic (Fe_3O_4) features into single entity nanostructures is reported through a facile method, using Fe_3O_4 as core nanoparticles, which were coated with SiO_2 shell and further grafted with Eu^{3+} and Tb^{3+} complexes. The sophisticated structural features and morphologies of the core-shell Fe_3O_4@SiO_2-(TTA-RE-L) nanomaterials were studied by Small-angle X-ray Scattering. The core mean size $\langle D_{SAXS}\rangle$, shell thickness ΔR, cluster size ξ and fractal dimension D_F were determined by fitting the experimental SAXS data, corroborating through Transmission Electron Microscopy images. The DC magnetic properties at temperatures of 2 and 300 K were explored in support to the structural conclusions from SAXS and TEM analyses. The magnetic contributions of the RE^{3+} ions to the magnetizations of the Eu^{3+} and Tb^{3+} nanocomposites were discussed. The photoluminescence properties of the Eu^{3+} and Tb^{3+} nanocomposites based on the emission spectral data and luminescence decay curves were studied. The experimental intensity parameters (Ω_λ), lifetimes (τ), emission quantum efficiencies (η) as well as radiative (A_{rad}) and non-radiative (A_{nrad}) decay rates were calculated and discussed, in addition, the structural conclusions from the values of the 4f-4f intensity parameters in the case of the Eu^{3+} ion. These novel Eu^{3+} and Tb^{3+} nanocomposites may act as red and green emitting layers for magnetic and light converting molecular devices.

1. Introduction

Progress in design and fabrication of bifunctional nanosized materials containing magnetic and photonic features integrated into a single entity nanostructures has been advanced rapidly [1], because of their potential multimodal biomedical applications such as: drug delivery carriers [2], photothermal destruction of tumor cells [3], MRI contrast agents [4,5], quantitative DNA analyses [6,7] and magnetic hyperthermia for cancer therapies [8,9]. Therefore, several reports have focused on preparation and characterization of multifunctional magnetic and fluorescent core-shell materials [10,11] as well as magnetite and trivalent rare earth ions (RE^{3+}) based magnetic and luminescent ones [1,12–14].

Among the iron oxides nanoscale particles, the Fe_3O_4 shows stronger magnetization, however, due to the large surface to volume ratio and high magnetization; bare magnetite nanoparticles are usually prone to aggregation [15]. This difficulty makes them inadequate candidates for biological applications. To overcome this drawback, coating with organic ligands, polymers and silica is often employed [16]. Nevertheless, the superparamagnetism of the Fe_3O_4 nanoparticles are also dependent on the surface modification [17,18], influencing the saturation magnetization, coercivity and blocking temperature [19,20] of these nanoparticles.

The silica coating is a most promising approach, presenting not only the encapsulated magnetite nanoparticles a biocompatibility [21], but also a greater chemical and mechanical stability against variation in pH and temperature [22]. Besides, SiO_2 coating retards the oxidation of Fe_3O_4 nanocrystals to α-Fe_2O_3 at high temperature

* Corresponding author.
E-mail addresses: latifkhn@iq.usp.br (L.U. Khan), hefbrito@iq.usp.br (H.F. Brito).

http://dx.doi.org/10.1016/j.jallcom.2016.06.009
0925-8388/

[23]. The surface of silica shell can be further functionalized to label with fluorescent dye molecules [24] and also introduce specific ligand functional groups to graft with the RE^{3+} complexes [13] to produce multifunctional optical and magnetic nanomaterials.

The interest in luminescent materials containing RE^{3+} ions has been grown considerably due to their unique ability to exhibit well-defined narrow emission bands in different spectral ranges from visible to near-infrared with relatively long lifetimes and high quantum yields [25]. These features make RE^{3+} materials efficient candidates for multidisciplinary photonic applications, recently extended from laser physics to materials sciences, optical markers, agriculture, and medical diagnostics [26], *etc.*

The photoluminescence properties of the RE^{3+} ions are mainly due to the 4f energy level structures, which are only slightly affected by the chemical environment due to the effective shielding of the 4f electrons by the external filled 5s and 5p sub-shells [25]. Therefore, the absorption and emission spectra of the 4f intra-configurational transitions of the RE^{3+} ions retain more or less their atomic character and similar irrespective of the host matrix or organic ligand [27].

The rare earth complexes can be remarkable candidates for light conversion molecular devices (LCMDs), since introducing the intramolecular energy transfer from the organic ligands to RE^{3+} ions (*antenna effect*) [28] and overcoming the problem of very low molar absorption coefficients (1.0 M^{-1} cm^{-1}) [27] of 4f-4f transitions. Therefore, the designs of efficient luminescent RE^{3+} complexes have become an important research subject [29], being investigated extensively using different organic ligands as sensitizers [30].

The RE^{3+} ions are paramagnetic due to the presence of unpaired electrons with the exception of La^{3+}, Lu^{3+} and Y^{3+} ones. Their magnetic properties are determined entirely by the ground state (except for the Sm^{3+} and Eu^{3+} ions), as the excited states are so well separated from the ground state due to the spin–orbit coupling and are thermally inaccessible [31]. The magnetic moment of the RE^{3+} ions is essentially independent of chemical environment and one cannot distinguish between different coordination geometries. However, the magnetic moments of the rare earth ions also contribute to the whole magnetization of the bifunctional nanomaterials [1].

In the present work, the syntheses, structural and morphological characterizations as well as optical and magnetic properties are reported for the bifunctional Fe_3O_4@SiO_2-(TTA-RE-L) (RE: Eu^{3+} and Tb^{3+}) nanocomposites with different organic ligands (L), where L: thenoyltrifluoroacetonate (TTA), Thioglycolate (TC), 4-aminobenzoate (AB) and 4-(aminomethyl)benzoate (AMB). The Small-angle X-ray Scattering (SAXS) data in support with Transmission Electron Microscopy (TEM) images were used to determine the structural features and morphology of the core-shell Fe_3O_4@-SiO_2-(TTA-RE-L) nanomaterials containing aggregation of Fe_3O_4 core nanoparticles. In addition, core mean size $\langle D_{SAXS} \rangle$, shell thickness ΔR, cluster size ξ and fractal dimension D_F for these nanocomposites were also calculated and discussed. Based on these structural and morphological data, the DC magnetic properties were studied at room (300 K) and low (2 K) temperatures in order to better understand the final structure of the optical and magnetic nanocomposites. The influences of amorphous silica phase and RE^{3+} complexes on the behavior of magnetization (M), coercive field (H_C) and blocking temperature (T_B) were presented and discussed. In addition, the magnetic contribution of the of RE^{3+} ions to the whole magnetization (M – H and ZFC/FC measurements) of the Eu^{3+} and Tb^{3+} nanomaterials was also studied. Though, the magnetite is usually a luminescence quencher, this difficulty was overcome by coating the Fe_3O_4 nanoparticles with silica shell using modified *Stöber method* [32]. The influence of the chemical structure of the ligand on the photoluminescence properties of the Eu^{3+} and Tb^{3+} ions was also studied to produce highly luminescent nanomaterials. The experimental intensity parameters (Ω_2 and Ω_4), radiative and non-radiative rates (A_{rad} and A_{nrad}) for the Eu^{3+} nanophosphors were calculated. Finally, the emission spectral features, the experimental emission quantum efficiencies (η) and the emission lifetimes for these nanomaterials are also discussed.

2. Experimental section

2.1. Reagents

The following commercially available chemical reagents were used without further purification. The $FeCl_3 \cdot 6H_2O$ and $FeCl_2 \cdot 4H_2O$ were purchased from Synth as well as Tetraethyl orthosilicate (TEOS), 3-Chloropropyl-triethoxysilane (CPTES), thenoyltrifluoroacetone (HTTA), 4-aminobenzoic acid (ABA) and 4-aminomethyl benzoic acid (AMBA) from Sigma-Aldrich. The Thioglycolic acid (TCA) was purchased from Merck as well as $EuCl_3 \cdot 6H_2O$ and $TbCl_3 \cdot 6H_2O$ were synthesized from the Eu_2O_3 and Tb_4O_7 (99.99% CSTARM) and hydrochloric acid (VETEC).

2.2. Materials preparation

Fe_3O_4 nanoparticles – The magnetite was prepared with chemical co-precipitation according to the reported literature procedure [33,34]. Each 50 mL solution of $FeCl_2$ (1.00 mol L^{-1}) and $FeCl_3$ (1.75 mol L^{-1}) in Milli-Q water was prepared separately into two beakers and then transferred together to a 250 mL three-necked flask, stirred under dynamic N_2 with continuous flow. The reaction mixture was heated at 60 °C and $NH_3 \cdot H_2O$ (v/v 28–30%) was added dropwise until pH adjusted to 11. The suspension was immediately turned black, indicating the formation of magnetite. Furthermore, the reaction content was heated at 80 °C for 1 h. The black color precipitate was isolated from the reaction mixture by applying external magnet, washed three times with Milli-Q water, dried under reduced pressure, and stored in vacuum desiccator.

Fe_3O_4@SiO_2 nanoparticles – The nanomaterials were prepared by modified *Stöber method,* as reported in the literature [32–34]. The 2.0 g of Fe_3O_4 nanoparticles were suspended in 100 mL of distilled water, followed by addition of the mixture of 5.0 mL of CPTES, 15 mL of methanol and 5 mL of aqueous NaF solution (1%). After stirring the reaction mixture for 5 min, 30 mL of tetraethyl orthosilicate (TEOS) was added slowly and stirred for 48 h at room temperature. The resultant product was separated with permanent magnet and washed with ethanol and Milli-Q water, dried under reduced pressure and stored in vacuum desiccator.

TTA ligand grafted magnetic core-shell nanostructures (Fe_3O_4@SiO_2-TTA) – These nanostructures were prepared by functionalizing the surface of Fe_3O_4@SiO_2 nanoparticles with thenoyltrifluoroacetonate (TTA) ligand. The mixture of 0.5 g (2.25 mmol) of HTTA and 0.11 g (4.50 mmol) of NaH in dry DMF/THF (1:3, v/v) was stirred at room temperature for 30 min. Thereafter, 1.2 g of Fe_3O_4@SiO_2 was added and the reaction mixture was heated at reflux for 96 h. After cooling to room temperature, the Fe_3O_4@-SiO_2-TTA product was separated by applying external permanent magnet, washed with ethanol, Milli-Q water and chloroform to remove the excess TTA and then dried in vacuum desiccator to get dark brown color Fe_3O_4@SiO_2-TTA nanomaterials.

Fe_3O_4@SiO_2-(TTA-RE-L) – The core-shell luminescent and magnetic nanomaterials were synthesized by general procedure, involving the chemical preparation of RE^{3+} complexes on the surface of Fe_3O_4@SiO_2-TTA nanostructures. In a typical procedure, to a suspension of 0.12 g of Fe_3O_4@SiO_2-TTA in 30 mL of ethanol was added 0.36 g of the ligand (L). After stirring the solution for 10 min,

few drops of $NH_3 \cdot H_2O$ (28–30 v/v %) was added and heated at 50 °C. Subsequently, a solution of 0.5 equivalent (relative to ligand) of the hydrated rare earth chloride in ethanol was added dropwise with the adjustment of pH to 8 by dropwise addition of $NH_3 \cdot H_2O$ (28–30 v/v %). The reaction mixture was continuously stirred at 50 °C for 4 h, thereafter, the temperature was adjusted to ambient temperature and the reaction mixture was further stirred for overnight. The resultant products were collected by magnetic separation with permanent magnet and washed with ethanol, methanol, Milli-Q water and chloroform to remove the excess of RE^{3+} complex, then were dried under reduced pressure, and stored in vacuum desiccator.

2.3. Characterization

The nanomaterials were characterized by X-ray Powder Diffraction (XPD) patterns using a Rigaku Miniflex II diffractometer, $CuK_{\alpha 1}$ radiation (λ: 1.5406 Å) in the 2θ range of 10–80°. The infrared absorption spectra (FTIR) were measured using KBr pellet technique with a Bomem MB100 FTIR from 400 to 4000 cm^{-1}.

Transmission electron microscopy (TEM) images were measured with a JEOL JEM 2100 LaB6 TEM (acceleration voltage 200 kV, Spot Size 1, Alpha Selector 3) and JEOL JEM 3010 HR-TEM (acceleration voltage 300 kV, Spot Size 1, Alpha Selector 3). The nanoparticles were dispersed in Milli-Q water and sonicated for 15 min. Samples were prepared by drying the water-dispersed nanoparticles on a carbon-coated copper grid (ultrathin carbon/holey carbon, 400 mesh cooper grid). The TEM images were acquired with the sample on a single-tilt sample holder using Gatan MSC798 TV camera, Gatan Digital Micrograph and EMMENU programs.

Small-angle X-ray Scattering (SAXS) experiments were recorded at the Centro Nacional de Pesquisa em Energia e Materiais (CNPEM), Brazilian Synchrotron Light Laboratory (LNLS) Campinas, Brazil. The measurements were carried out at room temperature using the beamline SAXS 2 in the energy range from 6.0 to 11.0 keV. The scattering intensity was measured as function of momentum transfer vector q ($q = 4\pi \sin\theta/\lambda$), in the range from 0.05 to 1.3 nm^{-1}, being θ is the scattering angle. Data treatment was performed using the SASFit software package developed at the Paul Scherrer Institute (Switzerland).

DC magnetic properties were studied using a Quantum Design, MPMS XL, SQUID magnetometer. Zero Field Cooling/Field Cooling (ZFC/FC) measurements were done to characterize the static magnetic properties of the nanomaterials. The measurements were carried out as follows: the sample was first cooled down from 300 to 2 K in a zero magnetic field, then a static magnetic field of 50 Oe was applied and the magnetization was measured increasing the temperature up to room temperature (300 K). Subsequently, the samples were cooled down to 2 K under the same applied magnetic field (50 Oe) and the magnetization was measured while warming up the samples from 2 to 300 K. The magnetization as a function of the applied field between −2 and +2 T were measured at selected temperatures from 2 to 300 K.

The excitation and emission spectra of the Eu^{3+} and Tb^{3+} nanomaterials were recorded with a SPEX FL212 Fluorolog-2 spectrofluorometer using a 450 W Xenon lamp as an excitation source and two 0.22 m double grating SPEX 1680 monochromators for dispersing the radiation. Luminescence decay curves of the Eu^{3+} nanomaterials were measured using the SPEX 1934D phosphorimeter accessory attached to the 150 W pulsed Xenon lamp. The entire luminescence setup was fully controlled by a DM3000F spectroscopic computer program and the spectral intensities were automatically corrected for the photomultiplier (PMT) response.

3. Results and discussion

The bifunctional core-shell luminescent and magnetic nanocomposites were prepared by multi-step syntheses, utilizing Fe_3O_4 as precursor core particles [33,34], which were further coated with silica using 3-chloropropyl-triethoxysilane (CPTES) and tetraethyl orthosilicate (TEOS) [32–34]. The silica shell formation on Fe_3O_4 with this method is a very slow process from 12 to 48 h of mechanical stirring at room temperature. Nevertheless, results in Fe_3O_4@SiO_2 particles usually contain variable number of Fe_3O_4 cores even under optimal conditions [13,21]. In addition, heating of the reaction causes of formation of irregular morphology big magnetite-silica aggregates [21]. The Fe_3O_4@SiO_2 nanoparticles were further grafted with thenoyltrifluoroacetonate (TTA) ligand by chemical substitution of the chloro (Cl) present on the surface of them with TTA organic moiety. Subsequently, a series of RE^{3+} complexes were synthesized on the surface of Fe_3O_4@SiO_2-TTA nanostructures using different organic ligands (L), in order to saturate the first coordination sphere of the RE^{3+} ions. The schematic structure and stepwise preparation method of the bifunctional luminescent and magnetic nanomaterials are illustrated in the Scheme 1.

3.1. Structural and morphological characterization of Fe_3O_4@SiO_2-(TTA-RE-L)

The FTIR absorption spectra (Supplementary materials, Figs. S1 and S2) of the Fe_3O_4@SiO_2, Fe_3O_4@SiO_2-TTA and Fe_3O_4@SiO_2-(TTA-RE-L) nanomaterials are dominated by the broad absorption bands centered at *ca* 3500 cm^{-1}, indicating the presence of the water molecules in the nanomaterials. The absorption band centered at 1632 cm^{-1} corresponds to the $\nu_{C=O}$ of the thenoyltrifluoroacetonate (TTA) in the Fe_3O_4@SiO_2-TTA nanostructure. It was red shifted in the absorption spectrum of the Fe_3O_4@SiO_2-(TTA-Eu-TTA) nanomaterial and appeared at 1619 cm^{-1}, suggesting that the TTA is coordinated to the Eu^{3+} ion *via* oxygen atoms. Moreover, the infrared spectrum of the Fe_3O_4@SiO_2-(TTA-Eu-TC) shows an absorption band in the region of 1560–1665 cm^{-1} corresponds to the $\nu_{C=O}$ of carboxylic group of the thioglycolate (TC) ligand coordinated to the Eu^{3+}ion (see Supplementary materials, Fig. S1). In addition, the absorption bands observed at 1627 and 1637 cm^{-1} assigned to the $\nu_{C=O}$ of carboxylic group of the 4-Aminobenzoate (AB) and 4-Aminomethyl benzoate (AMB) ligands coordinated to the RE^{3+} ion in the Fe_3O_4@SiO_2-(TTA-RE-AB) and Fe_3O_4@SiO_2-(TTA-RE-AMB) nanocomposites, respectively. It was also observed the absorption bands in the region of 1412–1540 cm^{-1} correspond to the $\nu_{C=C}$ in aromatic ring of the TTA, AB and AMB ligands. Besides, the infrared absorption spectra of all the Fe_3O_4@SiO_2, Fe_3O_4@SiO_2-TTA and Fe_3O_4@SiO_2-TTA-RE-L) nanostructures present a strong absorption band at 1098 cm^{-1} corresponds to the stretching vibration of the framework and terminal *Si–O-* groups, confirming the coating of Fe_3O_4 nanoparticles with amorphous silica phase (Supplementary materials, Figs. S1 and S2). The weak absorption band observed at *ca* 595 cm^{-1} for the Fe_3O_4@SiO_2, Fe_3O_4@SiO_2-TTA nanostructures corresponds to the $\nu_{Fe\text{-}O}$ in the crystal lattice of Fe_3O_4 core is also maintained to certain extent in infrared spectra of the Fe_3O_4@SiO_2-(TTA-RE-L) nanocomposites.

The structures of the Fe_3O_4@SiO_2, Fe_3O_4@SiO_2-TTA and Fe_3O_4@SiO_2-(TTA-RE-L) nanomaterials were further characterized by X-ray powder diffraction (XPD) technique (Fig. 1 and Supplementary materials, Fig. S3). As shown in the XPD pattern of magnetite, the diffraction reflections can be indexed as the face-centered cubic (fcc) lattice of the Fe_3O_4 phase (XPD reference pattern of Fe_3O_4, ICDD/PDF 19–629). Therefore, the XPD patterns of the Fe_3O_4@SiO_2 and Fe_3O_4@SiO_2-TTA nanostructures retain the

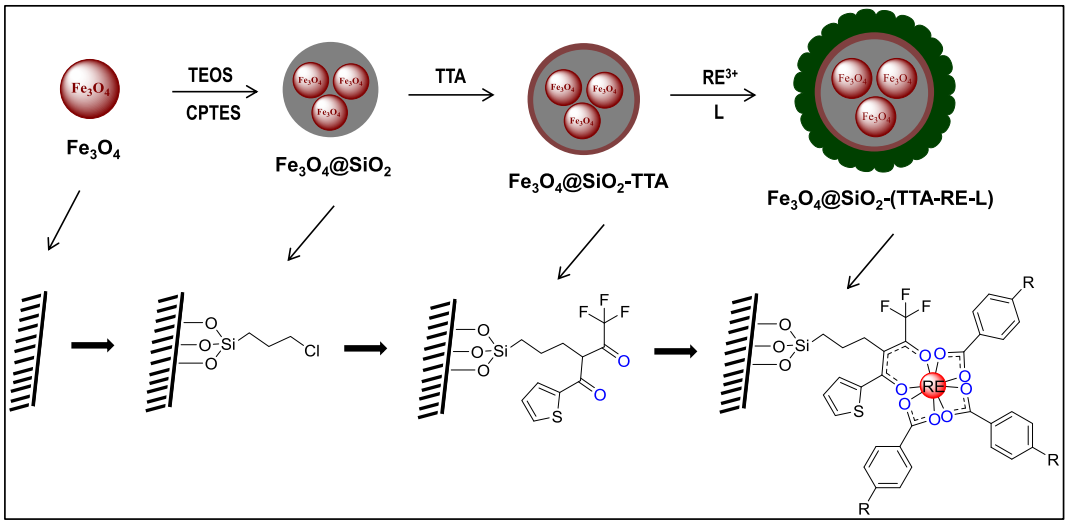

Scheme 1. Preparation route of magnetic and luminescent nanocomposites; including synthesis of Fe_3O_4@SiO_2 nanoparticles, chemical modification with TTA and further syntheses of RE^{3+} complexes on the surface of Fe_3O_4@SiO_2-TTA nanostructures - Fe_3O_4@SiO_2-(TTA-RE-L).

reflections of the Fe_3O_4 spinel structure, in addition, to the mainly characteristic reflection of an amorphous silica phase, confirming the coating of the magnetite core with silica shell (Fig. 1). However, the intensity of these characteristic reflections decreases due to the further grafting of Fe_3O_4@SiO_2 with TTA ligand as shown in diffraction pattern of Fe_3O_4@SiO_2-TTA. In the case of the Fe_3O_4@-SiO_2-(TTA-RE-L) nanocomposites, the characteristic reflections of the magnetite are no longer appeared due to domination by either the diffraction reflections or amorphous phase of the Eu^{3+} complexes, suggesting the efficient formation of rare earth complexes on the surface of Fe_3O_4@SiO_2-TTA nanostructure.

The mean crystallite size (D) of the precursor Fe_3O_4 core particles were deduced from the full width at half maximum (FWHM, β) of the most intense peak using Scherer's formula: $D = K\lambda/\beta cos\theta$, where K is the dimensionless shape factor, λ is the wavelength of the X-ray radiation employed ($CuK_{\alpha 1}$ radiation, λ: 1.5406 Å), θ is the diffraction angle (Bragg angle) and β is the full width at half maximum of the peak, in radians. The calculated mean crystallite size of the Fe_3O_4 nanoparticles was about 9 nm.

The morphology of the luminescent and magnetic nanomaterials was studied using the TEM and high-resolution TEM (HR-TEM) images (Fig. 2) of four selected materials. The nanoparticles with cubical and spherical shapes near 10 nm and well-defined crystallinity were observed for the bare Fe_3O_4, corroborating by the XPD pattern. For the Fe_3O_4@SiO_2, Fe_3O_4@SiO_2-(TTA-Tb-L) and Fe_3O_4@SiO_2-(TTA-Eu-L), biggest nanostructures composed of several magnetite nanoparticles (agglomerated) with the coating were observed (see also Supplementary materials Figs. S4–S7 for more images). Considering that TEM images only give local description on part of these nanomaterials, Small Angle X-Ray Scattering (SAXS) measurements were performed and the results were combined with the TEM and HR-TEM preliminary results, in order to globally understand the possible structures present on each Fe_3O_4@SiO_2, Fe_3O_4@SiO_2-TTA and Fe_3O_4@SiO_2-(TTA-RE-L) nanostructures.

Fig. 3 shows a *log* − *log* representation of scattering curves of the luminescent and magnetic nanocomposites, including the scattering curves of Fe_3O_4 and Fe_3O_4@SiO_2 nanoparticles, which are vertically shown for clarity. All the experimental scattering profiles (symbols) are slightly different, however all patterns display a power law comportment with a smooth decreasing q-behavior. These

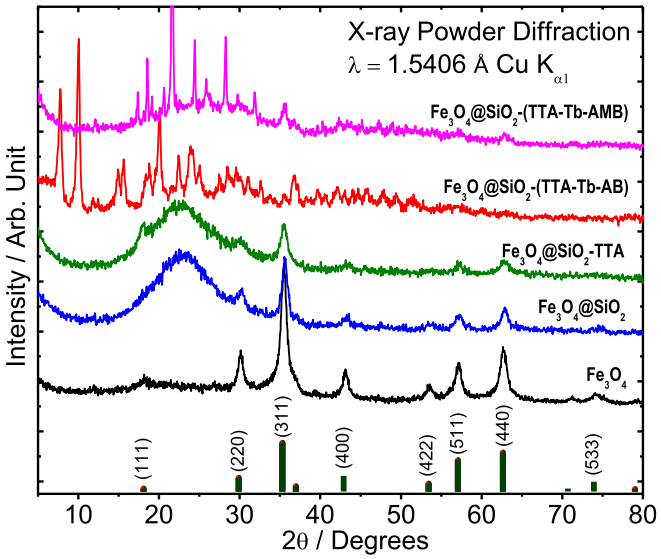

Fig. 1. X-Ray Powder Diffraction patterns of the Fe_3O_4, Fe_3O_4@SiO_2, Fe_3O_4@SiO_2-TTA and Fe_3O_4@SiO_2-(TTA-Tb-L) nanomaterials.

patterns are typical to interacting particulate systems, showing at low q region a clear deviation from the Guinier's law [35,36], indicating polydispersity and aggregation. Such deviation arises from the scattering interference between the neighboring Fe_3O_4 or Fe_3O_4@SiO_2 nanoparticles as the case. On the other hand, in the high q region, after background subtraction, all scattering profiles follow a power law behavior with a slope close to −4, representative of Porod scattering from the smooth surface of the elementary particles.

In order to take into account the single or core-shell nanoparticle aggregation, the experimental scattering curves were analyzed using the structure factor $S(q)$ derived from the fractal aggregate model, postulated by Chen and Teixeira [37]. This analytical function, $S(q)$, considers fractal aggregates composed of primary particles of radius R, with fractal dimension D_F and a limited aggregate size ξ. This structure factor is given by Eq. (1):

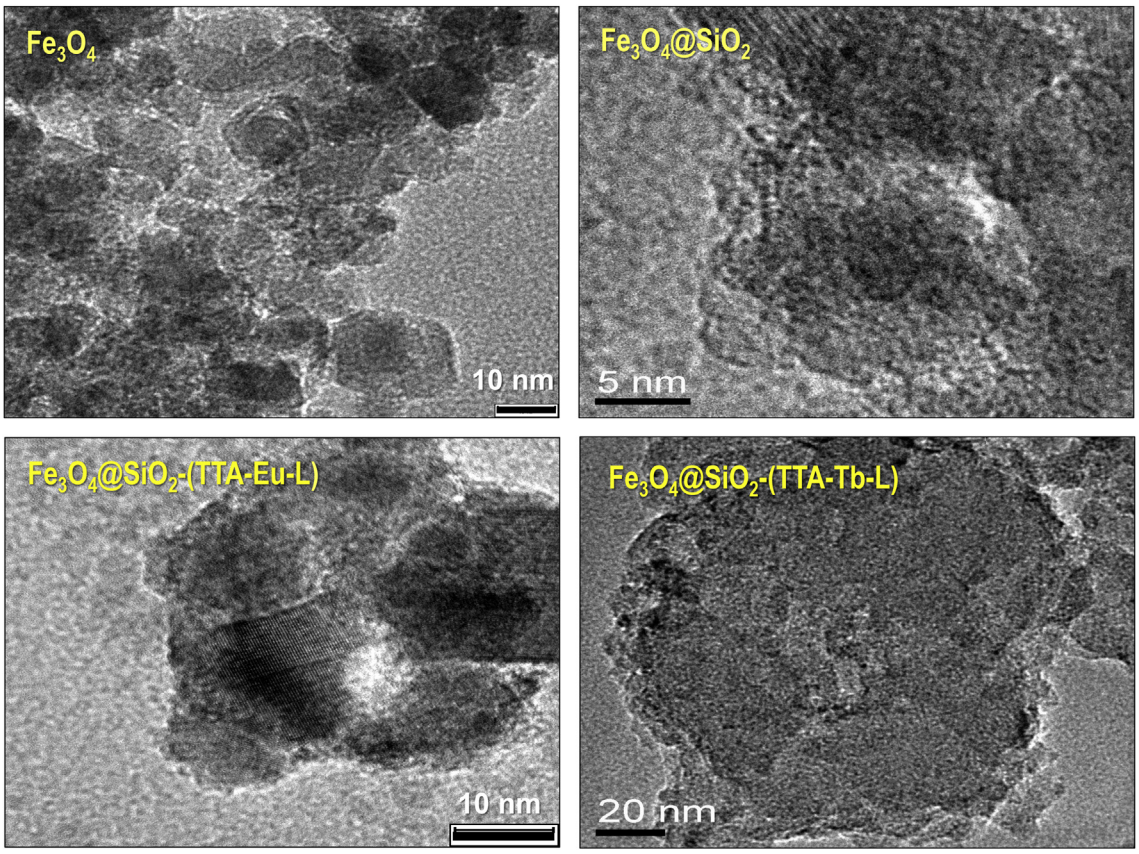

Fig. 2. TEM and High-resolution TEM images (clockwise from top left) of Fe_3O_4, Fe_3O_4@SiO_2, Fe_3O_4@SiO_2-(TTA-Eu-L) and Fe_3O_4@SiO_2-(TTA-Tb-L) nanomaterials.

$$S(q) = 1 + \frac{D_F \Gamma(D_F - 1)}{(qR)^{D_F}} \frac{\sin\left[(D_F - 1)\tan^{-1}(q\xi)\right]}{\left(1 + \frac{1}{(q\xi)^2}\right)^{\frac{(D_F-1)}{2}}} \quad (1)$$

Being $\Gamma(D_F - 1)$ is the gamma function.

The scattered intensity from a collection of particles can be described as the product of two contributions, the structure $S(q)$ and form $P(q)$ factors. For fitting procedure, to the product $S(q)P(q)$, was added a constant term (C_{BKG}), taking in account the incoherent background. In the case of the Fe_3O_4 nanoparticles, it was used a form factor for polydisperse spheres with mean radius size R, which is given by equation:

$$P(q, R, \Delta\eta) = \int_0^\infty K^2(q, R, \Delta\eta) f(R) dR,$$

where, $\Delta\eta$ is the scattering length density difference between nanoparticles and the solvent. On the other hand, for Fe_3O_4@SiO_2 nanoparticles and Fe_3O_4@SiO_2-(TTA-RE-L) nanocomposites, it was chosen the core shell form factor for polydisperse spherically symmetric particles with mean radius size R and shell thickness ΔR, such form factor is given by $P(q, R, \Delta R, \Delta\eta_1, \Delta\eta_2) = \int_0^\infty [K(q, R + \Delta R, \Delta\eta_2) - K(q, R, \Delta\eta_2 - \Delta\eta_1)]^2 f(R) dR$. In this equation $\Delta\eta_1$ and $\Delta\eta_2$ are the scattering length density difference between the core or shell and the solvent, respectively. In all cases $f(R)$ is the radii distribution of lognormal type [38] and $K = \frac{4}{3}\pi R^3 \Delta\eta 3 \frac{\sin(qR) - qR\cos(qR)}{(qR)^3}$.

SAXS fitted parameters are summarized in the Table 1. The obtained mean core sizes $\langle D_{SAXS} \rangle$ are smaller than those observed in the TEM images. The underestimation of the mean nanoparticle size is usual in aggregate nanoparticle systems and arises from the scattering interference between the neighboring nanoparticles [39,40]. Accordingly, it is possible to consider that for the Fe_3O_4 and Fe_3O_4@SiO_2 systems, the lowest *apparent size* values were obtained, attributing to the fact that the nanoparticles are closer to each other. On the other hand, when the surface of the Fe_3O_4@SiO_2 was further modified with –(TTA-Eu or Tb-L), the separation among the magnetic cores were promoted, and the achieved values of $\langle D_{SAXS} \rangle$ were found closer to the real ones. Such behavior is well correlated with the obtained shell thickness, where these values were 3.4 and 4.9 nm for Fe_3O_4@SiO_2 and Fe_3O_4@SiO_2-TTA nanostructures, respectively. While, for the Fe_3O_4@SiO_2-(TTA-Eu or Tb-L) nanocomposites were found the values of shell thickness (ΔR) higher than 17 nm (Table 1), correlating with the TEM images (see Supplementary materials, Figs. S4–S7). Maximum aggregated sizes are indicating the formation of aggregates in all the nanomaterials with values between 22 and 38 nm. Regarding the D_F values, fractal dimension remains almost constant for all the nanomaterials with values around 2.7, which is close to that predicted by the diffusion-limited cluster-cluster aggregation [41].

3.2. Magnetic properties

The magnetic properties (*M-H curves*) were measured at 300 and 2 K temperatures with the applied magnetic field cycling between +20 and −20 kOe (1 Oe = 79.577 Am^{-1}), respectively. The hysteresis loops of the Fe_3O_4, Fe_3O_4@SiO_2, Fe_3O_4@SiO_2-TTA and Fe_3O_4@SiO_2-(TTA-Eu-TC) nanomaterials (Fig. 4) as well as

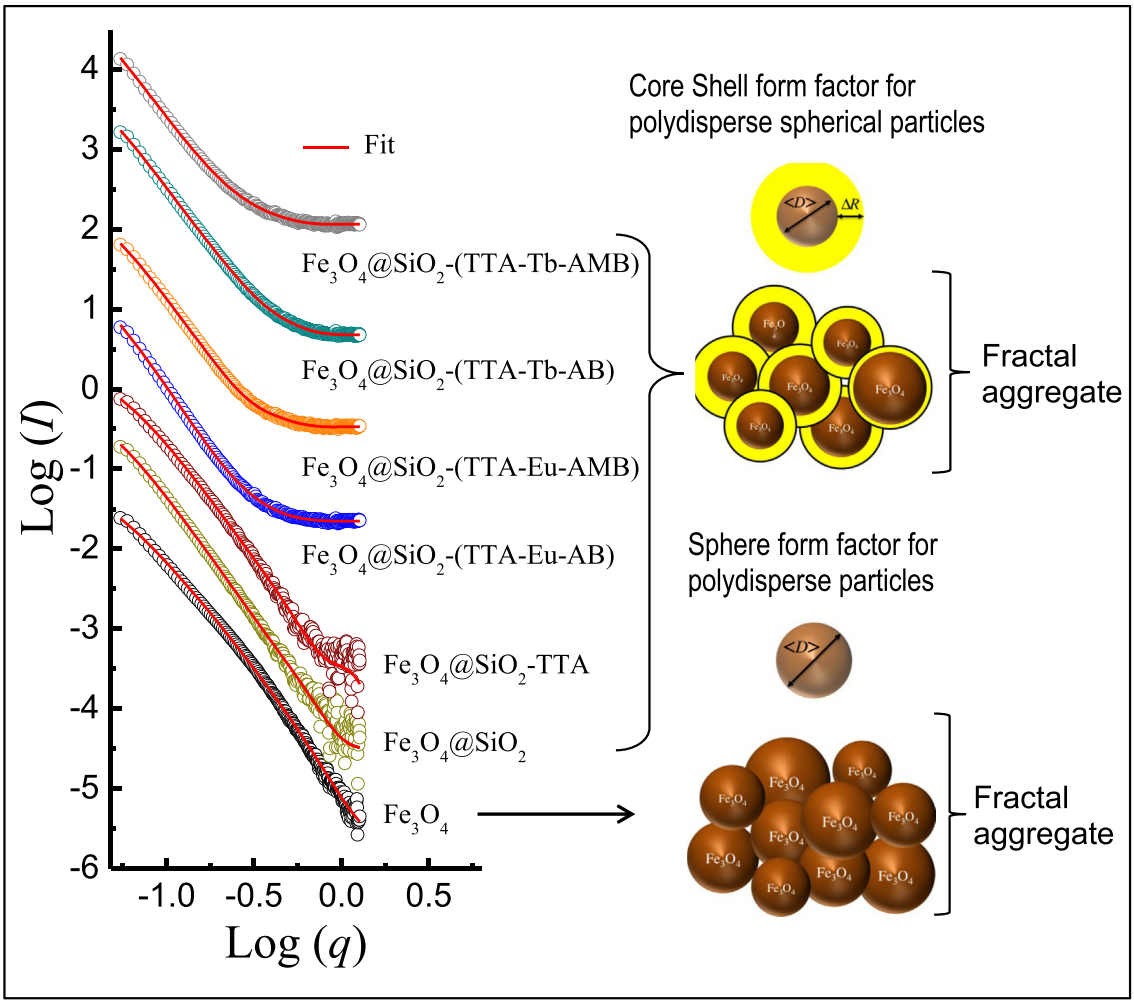

Fig. 3. *log–log* representation of scattering curves of the luminescent and magnetic nanocomposites, including the scattering curves of Fe_3O_4 and Fe_3O_4@SiO_2 nanoparticles. Schematic illustration of the structure formed by Fe_3O_4 and Fe_3O_4@SiO_2-(TTA-Eu/Tb-L) nanoparticles.

Table 1
SAXS fitted parameter data of the materials. Core mean size calculated using $\langle D_{SAXS}\rangle = 2R\exp(\sigma^2/2)$ being σ standard deviation of the lognormal size distributions, shell thickness ΔR, cluster size ξ and fractal dimension D_F.

Materials	$\langle D_{SAXS}\rangle$ Core (nm)	ΔR Shell (nm)	ξ (nm)	D_F
Fe_3O_4	4.2 ± 0.2	–	22.4 ± 0.3	2.5
Fe_3O_4@SiO_2	5.9 ± 0.2	3.4 ± 0.1	23.2 ± 0.3	2.7
Fe_3O_4@SiO_2-TTA	5.0 ± 0.2	4.9 ± 0.1	22.1 ± 0.3	2.6
Fe_3O_4@SiO_2-(TTA-Eu-AB)	9.1 ± 0.1	18.3 ± 0.1	29.2 ± 0.3	2.7
Fe_3O_4@SiO_2-(TTA-Eu-AMB)	9.8 ± 0.1	21.7 ± 0.1	25.0 ± 0.3	2.9
Fe_3O_4@SiO_2-(TTA-Tb-AB)	9.2 ± 0.1	17.4 ± 0.1	31.1 ± 0.3	2.8
Fe_3O_4@SiO_2-(TTA-Tb-AMB)	9.7 ± 0.1	27.8 ± 0.1	38.7 ± 0.3	2.7

Fe_3O_4@SiO_2-(TTA-Eu-AB), Fe_3O_4@SiO_2-(TTA-Eu-AMB), Fe_3O_4@SiO_2-(TTA-Tb-AB) and Fe_3O_4@SiO_2-(TTA-Tb-AMB) ones (Fig. 5) show a near superparamagnetic behavior at 300 K with null or very low value of coercive field (H_C). For the Fe_3O_4 nanoparticles, the magnetization per mass of material at $H = 20$ kOe and $T = 300$ K exhibits a value of 56.3 emu g^{-1}, consequently, after coating with the silica shell (Fe_3O_4@SiO_2) it was observed a considerably decreased to 9.8 emu g^{-1}, showing large amount of non-magnetic mass contribution from the silica shell. In addition, due to the additional grafting of Fe_3O_4@SiO_2 nanoparticles with TTA organic moiety, the magnetization at the same temperature and magnetic field was also largely decreased to a value near 1.0 emu g^{-1}.

Furthermore, functionalization of the surface of Fe_3O_4@SiO_2-TTA nanostructure with Eu^{3+} and Tb^{3+} complexes, using different organic ligands results in a magnetization per mass of material at $H = 20$ kOe and $T = 300$ K, presenting the values about 0.9, 0.88, 1.59, 3.01 and 3.40 emu g^{-1} for Fe_3O_4@SiO_2-(TTA-Eu-TC), Fe_3O_4@-SiO_2-(TTA-Eu-AB), Fe_3O_4@SiO_2-(TTA-Eu-AMB), Fe_3O_4@SiO_2-(TTA-Tb-AB) and Fe_3O_4@SiO_2-(TTA-Tb-AMB) nanocomposites, respectively (Table 2).

The observed decrease in magnetization values measured at $H = 20$ kOe and $T = 300$ K for the Fe_3O_4@SiO_2-TTA, as well as those ones functionalized with Eu^{3+} and Tb^{3+} complexes, when compared to the Fe_3O_4@SiO_2 nanostructure could be attributed to

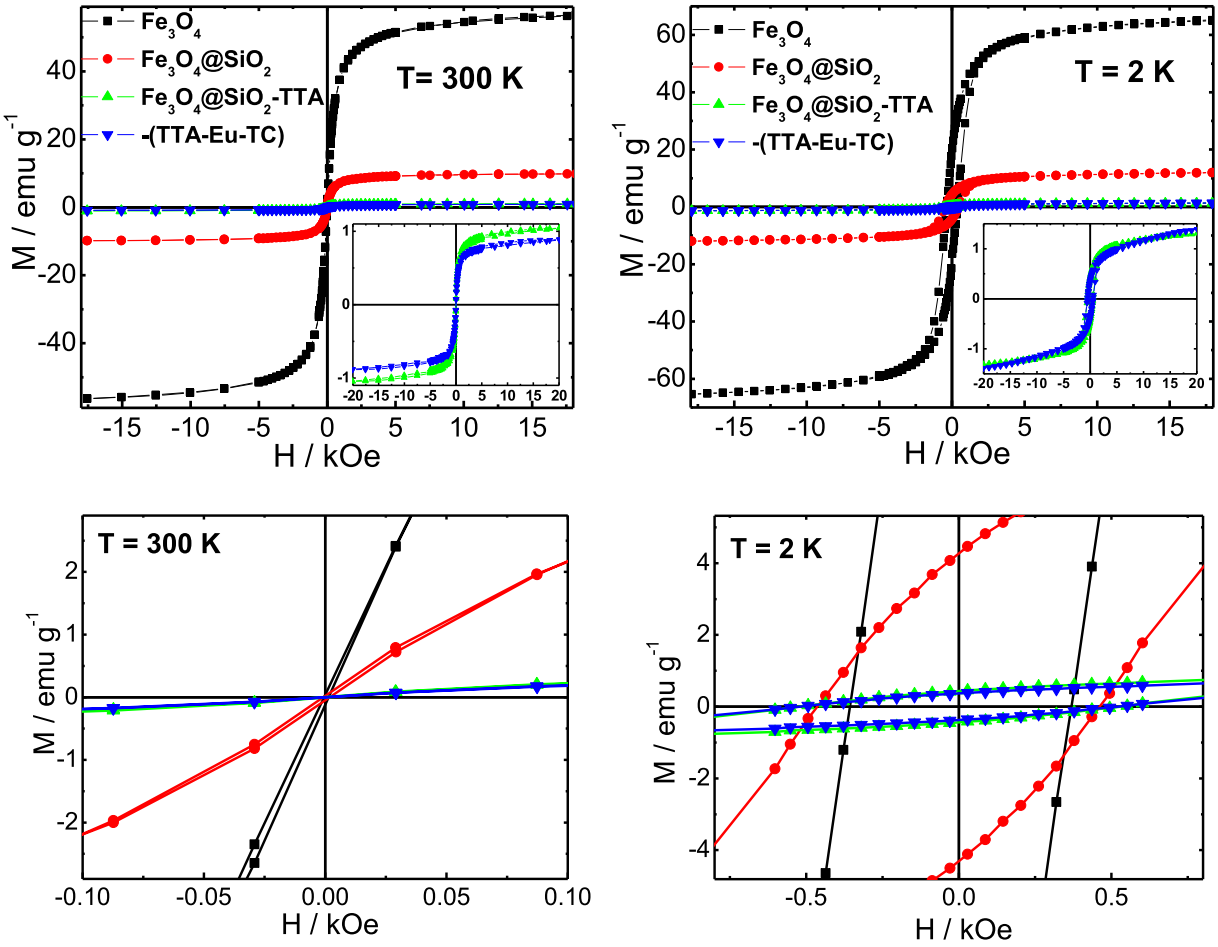

Fig. 4. Magnetization as a function of applied field (clockwise from top left) of the Fe_3O_4, Fe_3O_4@SiO_2, Fe_3O_4@SiO_2-TTA and Fe_3O_4@SiO_2-(TTA-Eu-TC) nanomaterials at room (300 K) and low temperature (2 K) as well as zoom-in of the *M-H curves* in low field regions.

the aspects, such as: *i*) reduction of the degree of crystalline order as indicated by XPD patterns or the *ii*) presence of silica shell and successive organic coating on the surface of Fe_3O_4@SiO_2 nanomaterial caused by chemical modification with TTA organic moiety and RE^{3+} complexes.

In this regard, the above mentioned magnetization values indicate that the silica shell and organic moieties contribute to a non-magnetic mass. In addition, the presence of almost zero coercivity and remanence on the magnetization curves indicate near superparamagnetic behavior at $T = 300$ K for the Fe_3O_4, Fe_3O_4@SiO_2 and Fe_3O_4@SiO_2-TTA as well as Eu^{3+} and Tb^{3+} nanomaterials. Interestingly, the successive increment of coercive field can be observed on the *M-H* curves of the magnetite nanoparticles with silica coating and further grafting with organic compound (TTA), without the nanocomposites containing RE^{3+} ions components.

At low temperature (2 K), the magnetic field dependence of the magnetization shows that Fe_3O_4@SiO_2 nanoparticles are reached larger magnetization values (Fig. 4), as was also reported by the G. Marcelo and co-workers [42] for this kind of nanosystems. The increase in coercive field was attributed to the surface effect induced by the silica that generates an extra energy term (possibly due to the surface spin freezing). The surface spin effect vanishes due to the functionalization of the RE^{3+} complexes on the surface of silica-coated magnetite nanoparticles. In addition, the temperature of the synthesis is leading to the surface spin relaxation. On the other hand, the *M-H* curves (Figs. 4 and 5) of all the nanomaterials show blocked regime at lower temperature. Indeed, the coercive fields recorded at $T = 2$ K increased considerably for the silica coated nanoparticles when compared the uncoated Fe_3O_4 ones and then also decreased when functionalized with the RE^{3+} complexes (Table 2).

Besides, the *M-H* curves recorded at $T = 2$ K (Fig. 5) show a similar trend in magnetic behavior for both Eu^{3+} and Tb^{3+} nanomaterials, as was observed at room temperature, with only slightly increase in the magnetization values (at $H = 20$ kOe) for the Tb^{3+} materials at 300 K. Although, the Fe_3O_4@SiO_2-(TTA-RE-AB) (RE: Eu and Tb) nanocomposites have the same ligand, this difference on magnetization could be attributed to higher magnetic moment of Tb^{3+} ion (9.8 Bohr magneton) than that of the Eu^{3+} ion (3.3 Bohr magneton).

The magnetization at high fields of the Tb^{3+} nanomaterials recorded at low temperature is considerably higher when compared to the Eu^{3+} counterpart ones. This magnetic behavior could be explained considering the difference of curie constants $(T_C \propto n(g_J \mu_B \sqrt{J(J+1)})^2/3k_B$, where n is the number of magnetic moment per unit volume, g_J is the Landé g-value, μ_B is the Bohr magneton, J the total angular momentum and k_B is the Boltzmann constant) of the europium and terbium ions. The $^5F_6$ ground state of the Tb^{3+} ion has total angular momentum (J = 6) and much higher curie constant when compared to the $^5F_0$ ground state of the Eu^{3+} ion with J = 0. Therefore, an abrupt increase in magnetic susceptibility of Fe_3O_4@SiO_2-(TTA-Tb-AB) and Fe_3O_4@SiO_2-(TTA-Tb-AMB) nanomaterials is observed at low temperatures and relatively high

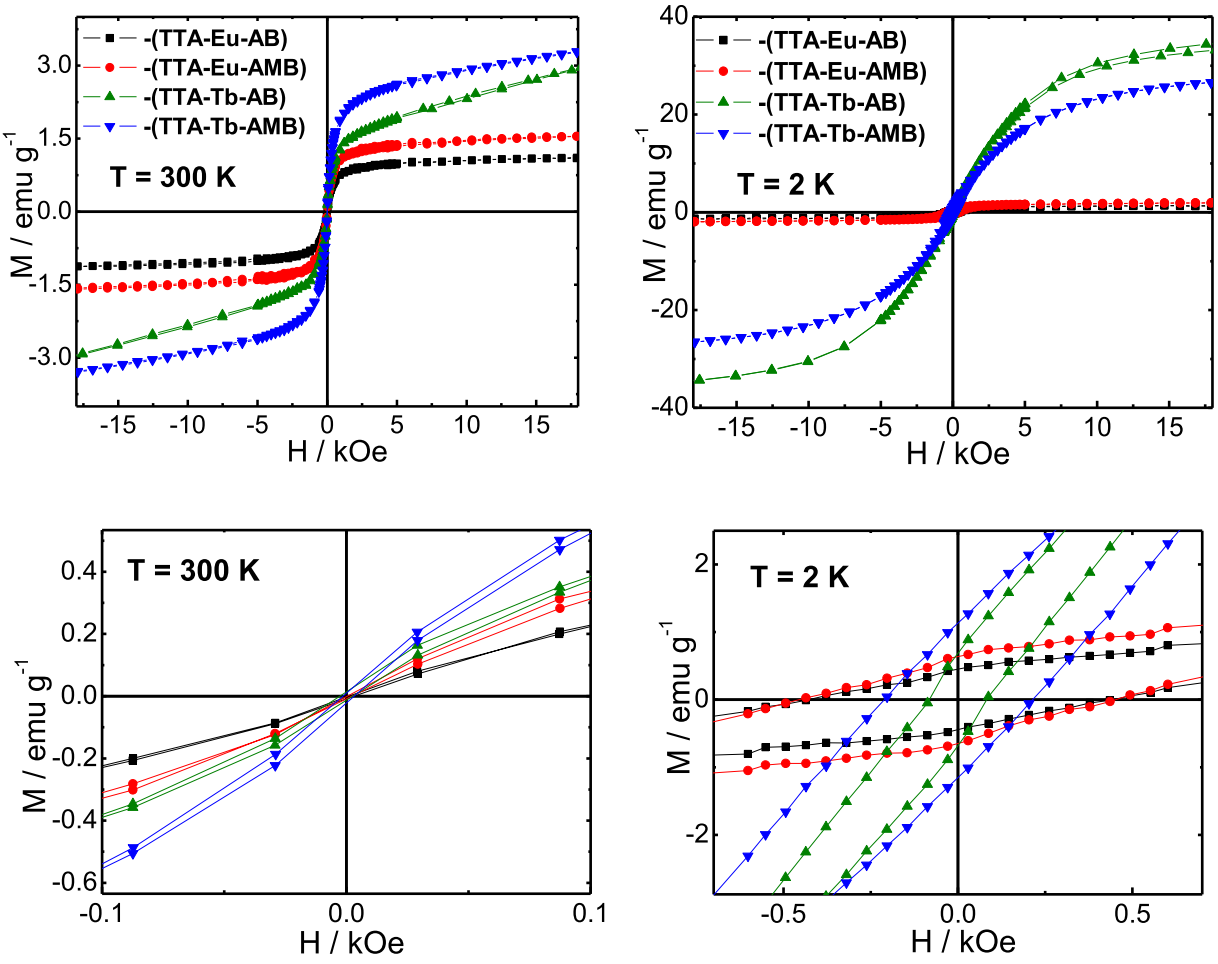

Fig. 5. Magnetization as a function of applied field (clockwise from top left) of the Fe_3O_4@SiO_2-(TTA-Eu-AB or AMB) and Fe_3O_4@SiO_2-(TTA-Tb-AB or AMB) nanocomposites at room (300 K) and low temperature (2 K) as well as zoom-in of the *M-H curves* in low field regions.

Table 2
Magnetization *(M)* and coercivity *(H_C)* magnetic parameters of Fe_3O_4, Fe_3O_4@SiO_2, Fe_3O_4@SiO_2-TTA and Fe_3O_4@SiO_2-(TTA-RE-L) at room (300 K) and low (2 K) temperatures.

Materials	M^{300K} (emu g^{-1})	M^{2K} (emu g^{-1})	H_C^{300K} (Oe)	H_C^{2K} (Oe)
Fe_3O_4	56.3	65.7	3	382
Fe_3O_4@SiO_2	9.8	12.1	13	463
Fe_3O_4@SiO_2-TTA	1	1.31	14	531
Fe_3O_4@SiO_2-(TTA-Eu-TC)	0.9	1.40	5	514
Fe_3O_4@SiO_2-(TTA-Eu-AB)	0.88	1.36	0	440
Fe_3O_4@SiO_2-(TTA-Eu-AMB)	1.59	1.90	0	460
Fe_3O_4@SiO_2-(TTA-Tb-AB)	3.01	34.90	2.6	83
Fe_3O_4@SiO_2-(TTA-Tb-AMB)	3.39	27.00	2	213

magnetic field (higher than 300 Oe). Although this could be an explanation, for a more quantitative analysis other factors should be taken into account. For example, the dipolar interaction between the magnetite core nanoparticles and the RE^{3+} ions, which can lead to the nanoparticles stronger coupling, generating a collective behavior.

The magnetization at $H = 20$ kOe for Fe_3O_4@SiO_2-(TTA-Tb-AB) and Fe_3O_4@SiO_2-(TTA-Tb-AMB) nanomaterials is increasing thoroughly with decreasing temperature and is more noticeable at 2 K (Table 2), indicating that the magnetic contribution from the Tb^{3+} ion cannot be neglected at low temperatures and high magnetic field (higher than 300 Oe).

The temperature dependence magnetization at the Zero Field Cooling (ZFC) and Field Cooling (FC) modes (Fig. 6) were measured with an applied field of 50 Oe, between 2 and 300 K temperatures for the Fe_3O_4, Fe_3O_4@SiO_2, Fe_3O_4@SiO_2-TTA and Fe_3O_4@SiO_2-(TTA-RE-L) nanomaterials. Although the shape of ZFC/FC magnetization curves are more like a collective assemble nanoparticles, from magnetization loops and due to the absence of coercive field the nanoparticles could be considered near superparamagnetic regime at room temperature with irreversibility near 300 K for all the cases. However, important differences on the ZFC ramp were observed for the different nanomaterials. For the Fe_3O_4 nanoparticles a well-defined maximum can be observed at 230 K, ascribing to the maximum blocking temperature. While the Fe_3O_4@SiO_2, Fe_3O_4@SiO_2-TTA and Fe_3O_4@SiO_2-(TTA-RE-L) nanomaterials do not show this behavior in the measure temperature interval, which could be related to the dipolar interaction among

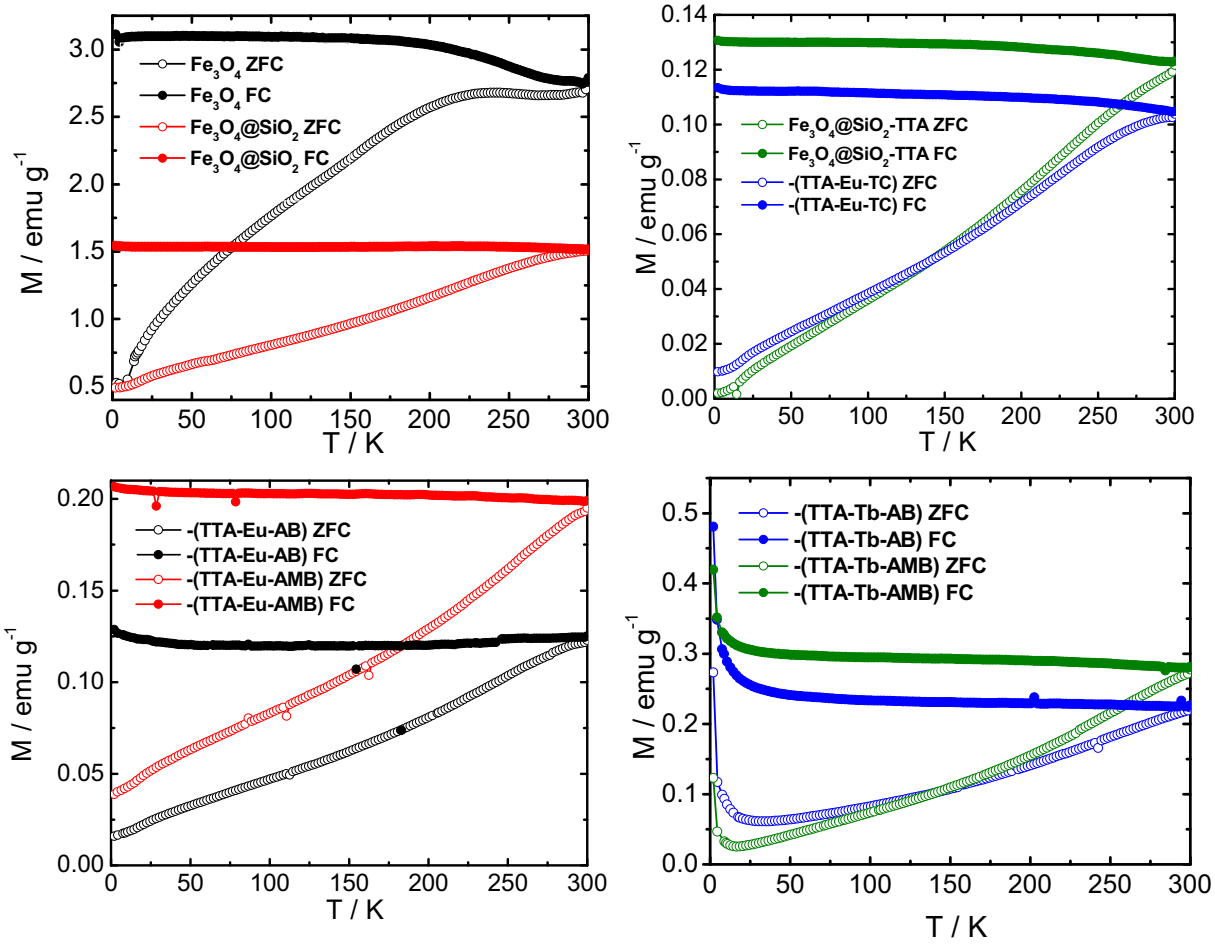

Fig. 6. Zero Field Cooling and Field Cooling measurements (clockwise from top left) of the Fe_3O_4, Fe_3O_4@SiO_2, Fe_3O_4@SiO_2-TTA and Fe_3O_4@SiO_2-(TTA-Eu-TC) nanomaterials as well as Fe_3O_4@SiO_2-(TTA-Eu-AB or AMB) and Fe_3O_4@SiO_2-(TTA-Tb-AB or AMB) nanocomposites at 50 Oe applied field.

the Fe_3O_4 core nanoparticles.

The dipolar interaction could be ascribed to the nanoparticles aggregation in the TEOS and CPTES solution during the SiO_2 coating process [21]. It is also interesting to notice the magnetization increase on the ZFC and FC curves of the Tb^{3+} nanomaterials recorded at 2 K, as the temperature further decreases (Fig. 6). This effect is due the paramagnetic contribution and higher magnetic moment of the Tb^{3+} ion compared to the other materials, including the Eu^{3+} ones; confirming the non-negligible effect of Tb^{3+} ion on magnetic properties.

3.3. Photoluminescence behavior

Among the luminescent trivalent rare earth materials reported in the literature [25,29], the Eu^{3+} and Tb^{3+} ions act as efficient emitting centers owing to the very intense red and green monochromatic colors displayed by their compounds, respectively. In addition, the principal emitting level ($^5D_0$) of the Eu^{3+} ion is non-degenerate showing the emission bands arising from the $^5D_0 \rightarrow {}^7F_J$ transitions (J = 0, 1, 2, 3 and 4) and can provide information about the local symmetry based on their ligand field splitting with a long lifetime of the emitting level. On the other hand, in contrast to the Eu^{3+} ion, detailed analyses of the energy level structure and site of symmetry of the chemical environment around the Tb^{3+} ion are complicated since the $^5D_4$ emitting level is ninefold degenerate. Generally, the organic ligand can act as sensitizer for both Eu^{3+} and Tb^{3+} ions due to their 4f intraconfigurational energy level structures through the *antenna effect*.

Fe_3O_4@SiO_2-(TTA-Gd-L) Phosphorescence – The energy positions of the excited triplet electronic states (T_1) of the organic ligands in rare earth complexes are important for the efficient intramolecular energy transfer to the RE^{3+} ions, in order to design highly luminescent materials. The great importance of using Gd^{3+} ion in these materials for the photoluminescence study is to determine the triple state (T_1) positions of the TTA, TC, AB and AMB organic ligands present on the surfaces of chemically modified core-shell nanoparticles.

The greater advantage of using the Gd^{3+} ion is due to concept that its compounds can simulate structural properties of the Eu^{3+} and Tb^{3+} complexes and also due to the first excited level ($^6P_{7/2}$) of Gd^{3+} ion is located at 32000 cm^{-1}, which is located above the T_1 state of the organic ligands [27,29]. Therefore, the Gd^{3+} ion cannot accept energy from the lower lying excited T_1 states of these ligands *via* intramolecular ligand-to-metal energy transfer. As a result, the emission spectra of the gadolinium complexes show only the phosphorescence from the T_1 states in lower energy than 320 nm, providing information about the structure of the energy levels of the corresponding ligands.

The emission spectra (see Supplementary materials, Fig. S8) of the Fe_3O_4@SiO_2-(TTA-Gd-L) nanocomposites (L: TTA, TC, AB and AMB) were recorded in the spectral range of 350–750 nm at 77 K, monitoring the excitation of the intraligand, $S_0 \rightarrow S_1$ transition of the TTA, TC, AB and AMB ligands correspond to the 370, 345, 315

and 282 nm, respectively. The emission spectrum of Fe_3O_4@SiO_2-(TTA-Gd-TTA) nanomaterial displays overlapped intense broad bands centered at 550 nm. The Fe_3O_4@SiO_2-(TTA-Gd-TC) nanophosphor also exhibits broad emission band with maximum centered at 500 nm. Moreover, the emission spectrum of Fe_3O_4@SiO_2-(TTA-Gd-AB) sample shows strong broad band with maximum at 463 nm, while the Fe_3O_4@SiO_2-(TTA-Gd-AMB) one displays strong emission band centered at 470 nm. The T_1 triplet state energies of the ligands in the Eu^{3+} and Tb^{3+} nanomaterials were estimated as the higher energy corresponding to the shortest emission wavelengths (0–0 phonon transition) on the basis of the phosphorescence spectra: 20746 (TTA), 23041 (TC), 23584 (AB) and 23364 cm^{-1} (AMB).

Fe_3O_4@SiO_2-(TTA-Eu-L) red phosphors – The excitation spectra (Fig. 7) of the Eu^{3+} nanophosphors in solid state were recorded at 77 K in spectral range of 240–550 nm, under the emission monitored at the $^5D_0 \rightarrow {}^7F_2$ hypersensitive transition of Eu^{3+} ion. These spectra are dominated by broad absorption bands centered at 372, 360, 362 and 282 nm, which are assigned to the $S_0 \rightarrow S_1$ transitions of TTA, TC, AB and AMB ligands, respectively. This result indicates that the luminescence from the Eu^{3+} nanophosphors is a consequence of sensitization of the europium excited state by energy transfer from the corresponding ligands and also due to the operative *antenna effect* of the β-diketonate (TTA moiety) present on the chemically modified surface of core-shell magnetic nanoparticles.

In addition, narrow absorption bands are also observed that can be assigned to the intraconfigurational-4f transitions, originating from the $^7F_0$ ground state to the following excited states of Eu^{3+} ion: $^5H_4$ (318 nm), $^5D_4$ (361 nm), $^5L_7$ (374 nm), $^5L_6$ (~394 nm), $^5D_2$ (~464 nm) and $^5D_1$ (~525 nm). However, these 4f-4f transitions are completely absent or negligibly smaller in the case of Fe_3O_4@SiO_2-(TTA-Eu-TTA) and Fe_3O_4@SiO_2-(TTA-Eu-AMB) nanophosphors (Fig. 7), suggesting that the luminescence sensitizations through intramolecular energy transfer from TTA and AMB ligands to Eu^{3+} ion are more efficient. The intensity of the large broad absorption bands are similar or comparably smaller to those of the 4f–4f narrow bands, as observed in excitation spectra of the Fe_3O_4@SiO_2-(TTA-Eu-TC) and Fe_3O_4@SiO_2-(TTA-Eu-AB) ones. Additionally, this result indicates that the second kind of ionic ligands play more important role in the *antenna effect* than the TTA group covalently bonded on the surfaces of Fe_3O_4@SiO_2 nanoparticles.

The emission spectra of all the europium nanomaterials were recorded in solid state at 77 K (Fig. 7) and room temperature (see Supplementary materials, Fig. S9), in the range of 500–750 nm, under excitation monitored at $S_0 \rightarrow S_1$ transition of each TTA, TC, AB and AMB ligands which is centered at 372, 360, 362 and 282 nm respectively. All of these spectra exhibit narrow emission bands assigned to $^5D_0 \rightarrow {}^7F_J$ transitions (where J = 0–4), with the $^5D_0 \rightarrow {}^7F_2$ hypersensitive one, that is centered at 612, 615, 615 and 612 nm for each Fe_3O_4@SiO_2-(TTA-Eu-TTA), Fe_3O_4@SiO_2-(TTA-Eu-TC), Fe_3O_4@SiO_2-(TTA-Eu-AB) and Fe_3O_4@SiO_2-(TTA-Eu-AMB) nanomaterials respectively (Fig. 7). It is important to mention that the emission spectra of all the Eu^{3+} nanomaterials no exhibit broad emission band from the triplet state (T_1) of the ligands, indicating an efficient ligand-to-metal intramolecular energy transfer [43,44]. In addition, the relative emission intensities of the $^5D_0 \rightarrow {}^7F_J$ transitions indicate that the Eu^{3+} ion is found in chemical environment without the center of inversion, considering that Laporte's rule is slightly relaxed for 4f–4f transitions due to the mixing of opposite parity electronic configurations [45], produced by the odd components of a non-centrosymmetric ligand field.

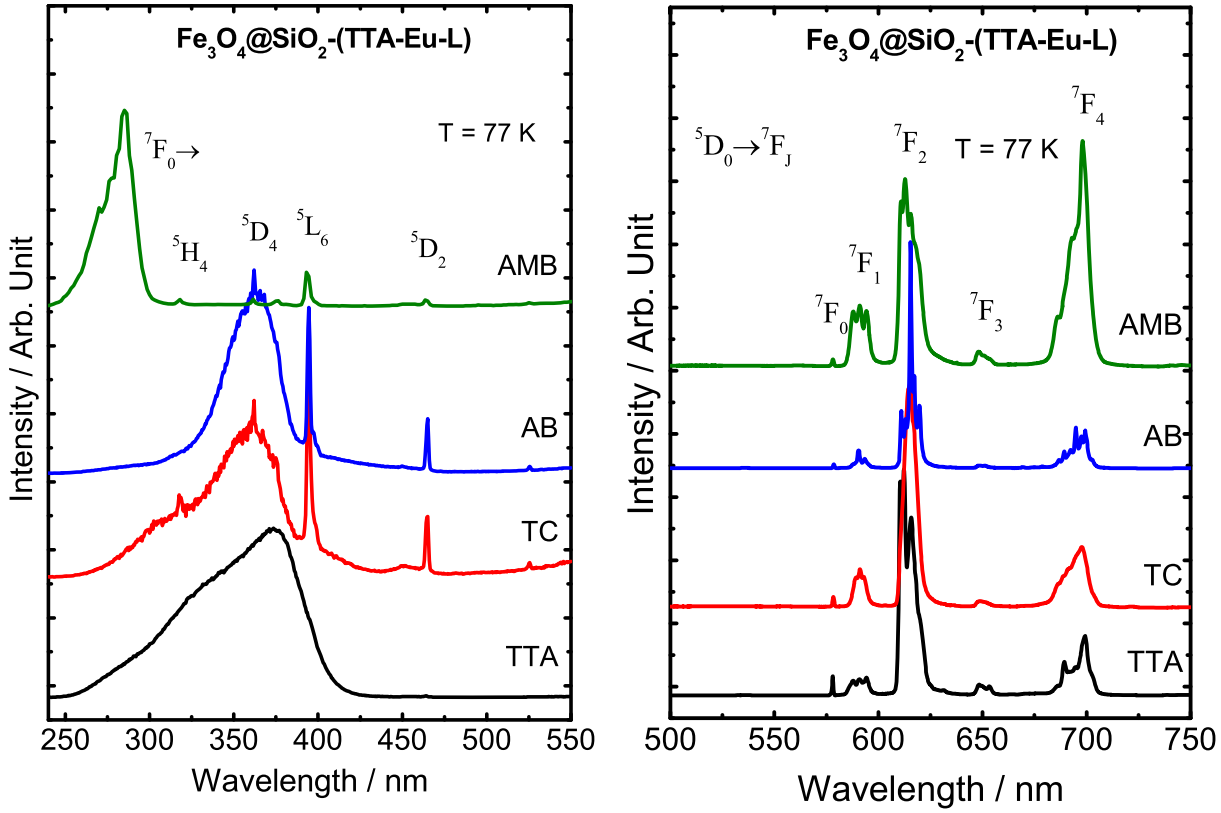

Fig. 7. Luminescence spectra of the Fe_3O_4@SiO_2-(TTA-Eu-L nanophosphors recorded at low temperature (77 K): excitation (left) spectra of monitoring the emission of the $^5D_0 \rightarrow {}^7F_2$ hypersensitive transition and emission (right) spectra under excitation at 372, 360, 362 and 282 nm, which correspond to the $S_0 \rightarrow S_1$ transition of the TTA, TC, AB and AMB ligands, respectively.

It was also observed the broadened emission bands of the $^5D_0 \rightarrow {}^7F_J$ transitions in the emission spectra of the Fe_3O_4@SiO_2-(TTA-Eu-TTA), Fe_3O_4@SiO_2-(TTA-Eu-TC), Fe_3O_4@SiO_2-(TTA-Eu-AB) and Fe_3O_4@SiO_2-(TTA-Eu-AMB) nanomaterials (Fig. 7), which can be explained by a non-homogeneity of Eu^{3+} sites due to the silica porous nanostructures, consistent with the previous reported result [46]. One of the effects of a distribution of different symmetry sites occupied by the RE^{3+} ion is to produce the inhomogeneous line broadening. The Stark levels overlap in such a way that in most cases, even the luminescence line-narrowing technique cannot help to identify a particular site occupied by the rare earth ion [47].

The most appealing result, that deserves to be mentioned here is the two main features observed in the emission spectrum of the Fe_3O_4@SiO_2-(TTA-Eu-AMB) nanophosphor. The first one is much lower intensity (practically negligible) of the $^5D_0 \rightarrow {}^7F_0$ transition, when it is allowed by symmetry; it "borrows intensity" mainly from the $^5D_0 \rightarrow {}^7F_2$ transition through the *J*-mixing effect. The second one is the abnormally high intensity of the $^5D_0 \rightarrow {}^7F_4$ transition, which contrary to the spectral data of other europium nanomaterials is as much intense as $^5D_0 \rightarrow {}^7F_2$ transition [48].

In order to interpret further this result and to obtain information about the chemical environment of the Eu^{3+} ion in the Fe_3O_4@SiO_2-(TTA-Eu-L) nanocomposites, experimental intensity parameters Ω_λ ($\lambda = 2$ and 4), radiative rates (A_{0J}) for the $^5D_0 \rightarrow {}^7F_2$ and $^5D_0 \rightarrow {}^7F_4$ transitions and emission quantum efficiency (η) were determined from their emission spectral data recorded at room temperature. The Ω_λ, also known as Judd-Ofelt parameters, which are determined from the intensities of the $^5D_0 \rightarrow {}^7F_J$ transitions ($J = 2$ and 4) of Eu^{3+} ion, and the forced electric dipole and dynamic coupling mechanisms are considered simultaneously. Under normal excitation conditions, the emission intensities (I) of the bands may be given by the expression [28]:

$$I_{0\rightarrow J} = \hbar\omega_{0\rightarrow J} A_{0\rightarrow J} N_0 \tag{2}$$

where $\hbar\omega_0$ is the energy of the transition (in cm^{-1}), N_0 is the population of the emitting $^5D_0$ level and $A_{0\rightarrow J}$ is the coefficients of spontaneous emission. For the experimental determination of the $A_{0\rightarrow J}$ emission coefficients from the emission spectra of the nanomaterials, the special character of the magnetic dipole allowed $^5D_0 \rightarrow {}^7F_1$ transition was exploited. This 4f-4f transition is formally insensitive to the chemical environment around the Eu^{3+} ion and consequently, can be used as a reference [28]. The values of Ω_λ are obtained from Eq. (3) as follow:

$$A_{0\rightarrow J} = \frac{4e^2\omega^3}{3\hbar c^3}\frac{1}{2J+1}\chi\sum_{\lambda=2,4,6}\Omega_\lambda\left\langle {}^5D_0\left\|U^{(\lambda)}\right\|{}^7F_J\right\rangle^2 \tag{3}$$

where $\chi = \frac{n_0(n_0^2+2)^2}{9}$ is the Lorentz local field correction and n_0 is the refractive index of the medium (n_0 assumed to be equal to 1.5). The squared reduced matrix elements $\left\langle {}^5D_0\left\|U^{(\lambda)}\right\|{}^7F_J\right\rangle^2$ have values of 0.0032 and 0.0023 for $J = 2$ and 4, respectively. The coefficients of spontaneous emission ($A_{0\rightarrow J}$) are then obtained from Eq. (4):

$$A_{0\rightarrow J} = \left(\frac{\sigma_{0\rightarrow 1}}{S_{0\rightarrow 1}}\right)\left(\frac{S_{0\rightarrow J}}{\sigma_{0\rightarrow J}}\right)A_{0\rightarrow 1} \tag{4}$$

where $S_{0\rightarrow J}$ corresponds to the integrated area under the curve related to the transition $^5D_0 \rightarrow {}^7F_J$ transition and $\sigma_{0\rightarrow J}$ is the energy barycenters of the transitions. The emission quantum efficiency (η) of the $^5D_0$ emitting level is determined according to the Eq. (5) [44,45]:

$$\eta = \frac{A_{rad}}{A_{rad} + A_{nrad}} \tag{5}$$

The total decay rate corresponds to $A_{tot} = \frac{1}{\tau} = A_{rad} + A_{nrad}$, where $A_{rad}(= \sum_J A_{0\rightarrow J})$ and A_{nrad} are the total radiative and non-radiative rates, respectively.

On the basis of theoretical considerations, the Ω_2 intensity parameter is by far mostly influenced by small angular changes in the local coordination geometry [1,48–50], while Ω_4 and mainly Ω_6 are by far the most sensitive to lanthanide-ligating atom bond distances. This fact together with changes in the ligating atoms polarizabilities (α) have been used to rationalize the hypersensitive character of certain 4f intraconfigurational transitions to changes in the chemical environment. The fact that the Ω_2 and Ω_4 experimental parameters of Fe_3O_4@SiO_2-(TTA-Eu-L) nanomaterials (L: TTA, TC, AB and AMB) (Table 3) have different values than for the [Eu-TTA-Si] materials reported by Lourenço [46] is an indication of different chemical environments and bond distances around the Eu^{3+} ion. The higher value of the Ω_2 experimental intensity parameter of the Fe_3O_4@SiO_2-(TTA-Eu-TTA) material (Table 3) reflects the higher intensity of the $^5D_0 \rightarrow {}^7F_2$ transition in this nanomaterial when compared to the $^5D_0 \rightarrow {}^7F_1$ transition intensity [48].

The abnormally high value of the Ω_4 (12×10^{-20} cm^2) parameter when compared to the Ω_2 (5×10^{-20} cm^2) experimental intensity parameter of the Fe_3O_4@SiO_2-(TTA-Eu-AMB) nanomaterial (Table 3) is to be noted. Malta and co-worker [48] have reported that this result may be theoretically interpreted in terms of the Ω_4 intensity parameter, and indicates that the local point symmetry is close to a distorted high symmetry one, D_{4d} in the present case, with a coordination number equal to 8.

The value of the emission quantum efficiency of the $^5D_0$ level for the Fe_3O_4@SiO_2-(TTA-Eu-TTA) nanophosphor ($\eta = 22\%$) is higher than the [Eu-TTA-Si] ($\eta = 16\%$) as shown in Table 3. This spectroscopic result is a consequence of the considerably increase radiative (A_{rad}) contribution to the total decay rate. Thus, corroborating the fact that the Eu-TTA is grafted to silica functionalized magnetite nanoparticles for the Fe_3O_4@SiO_2-(TTA-Eu-TTA) nanocomposite in contrast to the [Eu-TTA-Si], whereas, Eu-TTA complex is incorporated in silica matrix.

The high value of the emission quantum efficiency for Fe_3O_4@-SiO_2-(TTA-Eu-TC) nanophosphor ($\eta = 31\%$) when compared to the

Table 3
Experimental intensity parameters (Ω_λ), lifetimes τ, emission coefficient rates A_{rad} and A_{nrad} as well as emission quantum efficiencies η for the Fe_3O_4@SiO_2-TTA-Eu-L) nanocomposites.

Materials	Ω_2 (10^{-20} cm^2)	Ω_4 (10^{-20} cm^2)	A_{rad} (s^{-1})	A_{nrad} (s^{-1})	A_{tot} (s^{-1})	τ (ms)	η (%)
Fe_3O_4@SiO_2-(TTA-Eu-AB)	15	13	691	5931	6622	0.151	10
Fe_3O_4@SiO_2-(TTA-Eu-AMB)	5	12	390	1746	2136	0.468	18
Fe_3O_4@SiO_2-(TTA-Eu-TTA)	17	10	727	2478	3205	0.312	22
Fe_3O_4@SiO_2-(TTA-Eu-TC)	10	8	489	1054	1543	0.648	31
[Eu-TTA-Si][a]	8	9	410	2090	2500	0.400	16

[a] [46] $\tau_{average} = (A_1\tau_1^2) + (A_1\tau_1^2)/(A_1\tau_1 + A_2\tau_2)$, where τ_1 and τ_2 are short and long lifetimes, with corresponding intensity coefficients A_1 and A_2.

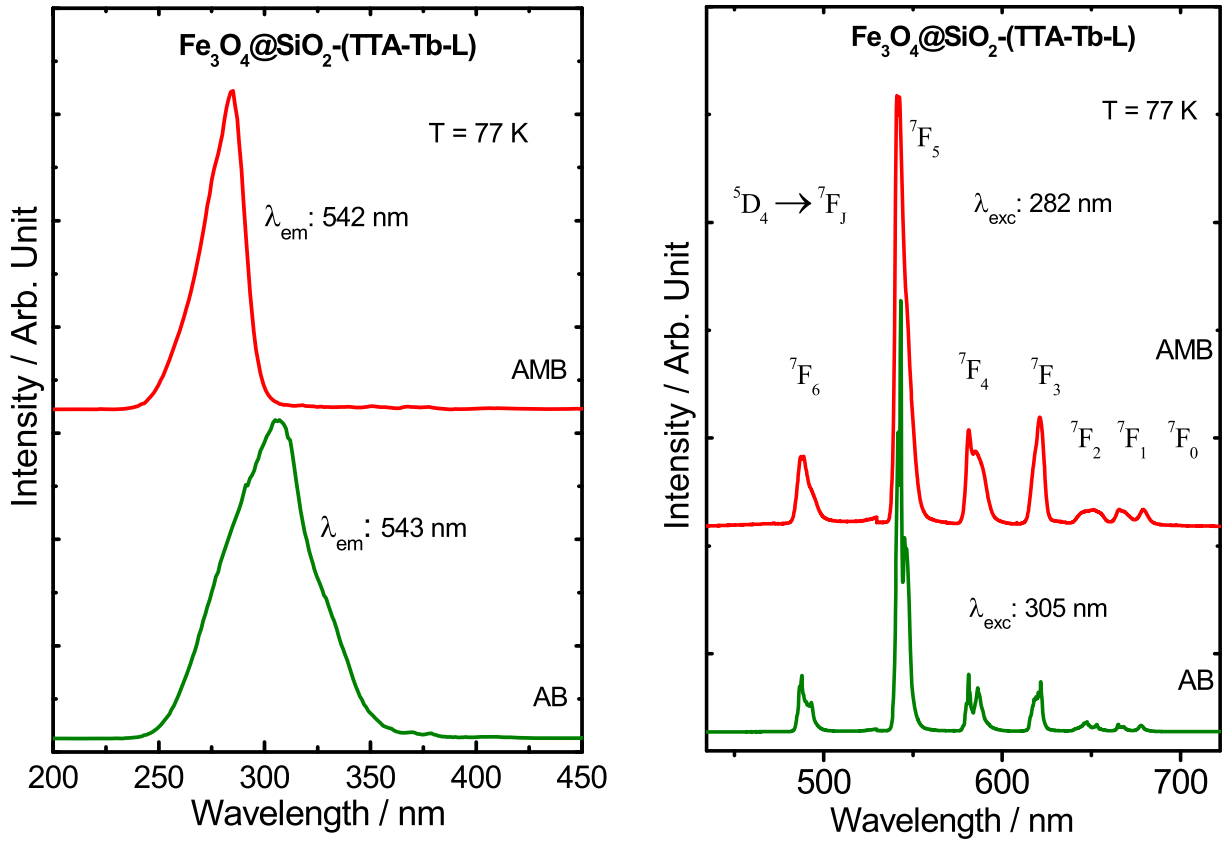

Fig. 8. Luminescence spectra of the Fe_3O_4@SiO_2-(TTA-Tb-L) nanophosphors recorded at low temperature (77 K): excitation (left) spectra of monitoring the emission of the $^5D_4 \rightarrow {}^7F_5$ hypersensitive transition and emission (right) spectra under excitation at 305 and 282 nm, which correspond to the $S_0 \rightarrow S_1$ transition of the AB and AMB ligands, respectively.

other prepared nanomaterials (Table 3) is a consequence of the presence of less water molecules in the materials. Where this fact is reflected by the lower contribution of non-radiative decay rate (A_{nrad}), arising from the OH oscillator of water molecules. On the other hand, the highest value of non-radiative decay rate for the Fe_3O_4@SiO_2-(TTA-Eu-AB) nanophosphor may be a consequence of the luminescence quenching *via* both water molecules oscillators and ligand-to-metal charge transfer (LMCT) state of the AB organic moiety. In this case, both of complementary effects can be contributed to the lowest value of emission quantum efficiency ($\eta = 10\%$) for the nanomaterial.

Fe_3O_4@SiO_2-(TTA-Tb-L) green phosphors – The excitation spectra (Fig. 8) of the terbium nanocomposites were recorded in the range of 200–450 nm at liquid nitrogen temperature, under emission monitored at the higher intensity $^5D_4 \rightarrow {}^7F_5$ transition of the Tb^{3+} ion. The excitation spectrum of Fe_3O_4@SiO_2-(TTA-Tb-AB) nanophosphor contains intense broad band centered at 305 nm corresponding to the $S_0 \rightarrow S_1$ transition of the AB ligand. Similarly spectrum of the Fe_3O_4@SiO_2-(TTA-Tb-AMB) one presents a broad absorption band at 282 nm attributed to the $S_0 \rightarrow S_1$ transition of AMB ligand.

The excitation spectra of both the nanomaterials (Fig. 8) no exhibit the narrow absorption lines due to $4f^8$-$4f^8$ transitions of the Tb^{3+} ion. As a result, it can be suggested that the Fe_3O_4@SiO_2-(TTA-Tb-AB) and Fe_3O_4@SiO_2-(TTA-Tb-AMB) nanomaterials act as green phosphors due to high efficient intramolecular energy transfer from the corresponding AB and AMB ligands to the terbium ion.

The emission spectra of the Fe_3O_4@SiO_2-(TTA-Tb-AB) and Fe_3O_4@SiO_2-(TTA-Tb-AMB) nanomaterials were recorded in the range of 400–750 nm at liquid nitrogen (Fig. 8) and room temperatures (see Supplementary materials, Fig. S10), under excitation at around 305 and 282 nm, assigned to the $S_0 \rightarrow S_1$ transitions of the AB and AMB ligands, respectively. The emission peaks were assigned to the $^5D_4 \rightarrow {}^7F_J$ transitions (J = 6, 5, 4, 3, 2, 1 and 0) of the Tb^{3+} ion. The optical data show that the $^5D_4 \rightarrow {}^7F_5$ transition at around 542 nm is the most intense one for Fe_3O_4@SiO_2-(TTA-Tb-AB) and Fe_3O_4@SiO_2-(TTA-Tb-AMB) nanomaterials, respectively.

In addition, the phosphorescence broadened band of the ligands were not observed in emission spectra of both nanomaterials, indicating a very operative intramolecular energy transfers from AB and AMB ligands to the Tb^{3+} ion. As similar to the Fe_3O_4@SiO_2-(TTA-Eu-L) nanophosphors, same pattern of broadened emission peaks were also maintained in the spectral features of the Tb^{3+} nanocomposites, corroborating the above mentioned result that produce the inhomogeneous line broadening. In the Fe_3O_4@SiO_2-(TTA-Tb-AB) and Fe_3O_4@SiO_2-(TTA-Tb-AMB) emission spectra line-narrowing technique cannot help to identify a particular site occupied by the trivalent terbium ion.

CIE chromaticity diagram – The chromaticity properties of the red and green emitting superparamagnetic Fe_3O_4@SiO_2-(TTA-Eu-L) and Fe_3O_4@SiO_2-(TTA-Tb-L) nanocomposites were studied using CIE chromaticity diagram (*Commission Internationale de l'Eclairage*) [51]. The Fe_3O_4@SiO_2-(TTA-Eu-L) nanophosphors show shift in the *x,y* color coordinates from the red to blue region due to the influence of SiO_2 matrix, consistent with previous reported result [46]. Thus, the (*x,y*) color coordinates ($x = 0.5649$ and $y = 0.2917$), ($x = 0.5444$ and $y = 0.2913$), ($x = 0.5139$ and $y = 0.2820$) and ($x = 0.6091$ and $y = 0.2937$) were calculated for the Fe_3O_4@SiO_2-

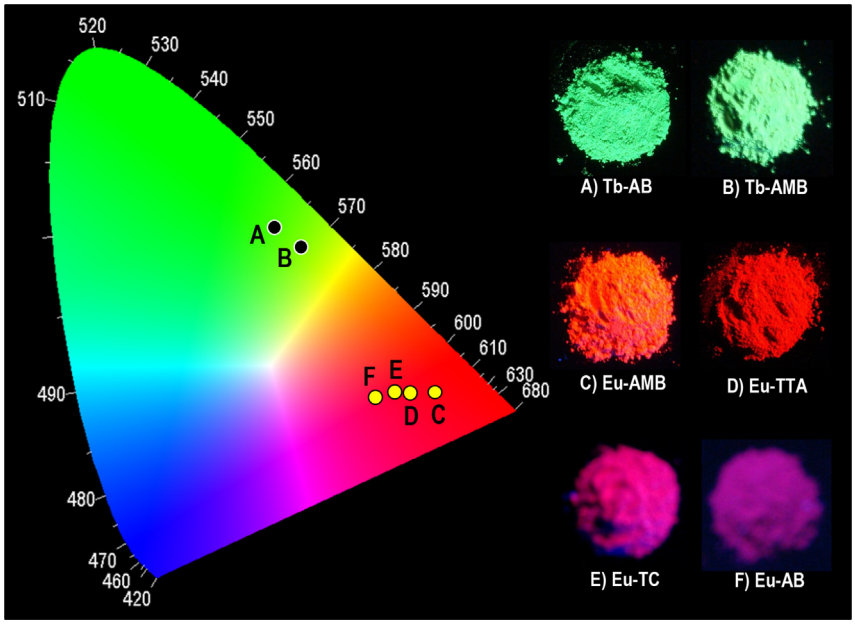

Fig. 9. CIE chromaticity diagram showing the (*x*,*y*) emission color coordinates for the Fe_3O_4@SiO_2-(TTA-Eu-L) and Fe_3O_4@SiO_2-(TTA-Tb-L) (L: AB, AMB, TTA and TC) nanophosphors irradiated at different wavelengths. The inset figures are photographs of nanomaterials taken with a digital camera displaying the green and red emissions under UV irradiation lamp at 254 and 365 nm. (For interpretation of the references to color in this figure legend, the reader is referred to the web version of this article.)

(TTA-Eu-TTA), Fe_3O_4@SiO_2-(TTA-Eu-TC), Fe_3O_4@SiO_2-(TTA-Eu-AB) and Fe_3O_4@SiO_2-(TTA-Eu-AMB) nanophosphors, respectively. The higher blue shift in *x*,*y* color coordinates of the Fe_3O_4@SiO_2-(TTA-Eu-AB) and Fe_3O_4@SiO_2-(TTA-Eu-TC) nanomaterials when compared to Fe_3O_4@SiO_2-(TTA-Eu-TTA) and Fe_3O_4@SiO_2-(TTA-Eu-AMB) ones is due to the lower red (Eu^{3+}) emission intensity of these nanomaterials (Fig. 9).

On the other hand, the Fe_3O_4@SiO_2-(TTA-Tb-AMB) nanomaterial displays green yellowish emission color with (x = 0.3984 and y = 0.5187) color coordinates when compared to the Fe_3O_4@SiO_2-(TTA-Tb-AB) one with (x = 0.3562 and y = 0.5466) color coordinates due to the $^5D_4 \rightarrow {}^7F_{6\text{-}0}$ transitions of the Tb^{3+} ion (Fig. 9). Thus, for the Fe_3O_4@SiO_2-(TTA-Tb-AMB) nanophosphor, a gradual shifting in the (*x*,*y*) color coordinates is observed from the green to the yellow spectral region due to the increased emission intensity contribution from the ^7F_J energy levels (J = 6, 5, 4 and 3) of Tb^{3+} ion. As a result, these luminescent and superparamagnetic nanomaterials also can act as efficient phosphors for magnetic and light conversion molecular devices (MLCMDs), displaying red and green emission colors arising from Eu^{3+} and Tb^{3+} ions (see Supplementary materials, Fig. S11).

4. Conclusion

The red-green emitting and magnetic nanocomposites containing Eu^{3+} and Tb^{3+} ions were successfully prepared by multistep syntheses, utilizing Fe_3O_4@SiO_2 nanostructures grafted with Eu^{3+} and Tb^{3+}complexes. The structural features and morphologies of these core-shell Fe_3O_4@SiO_2-(TTA-RE-L) nanocomposites were studied using SAXS, XPD and TEM analyses, as well as the average crystallite size of the Fe_3O_4 core nanoparticles were found near 10 nm. The SAXS data suggest that the bifunctional nanocomposites show sophisticated core-shell structure, containing fractal aggregates formed by cubical and spherical Fe_3O_4 core particles that support the DC magnetic properties, also corroborated by the TEM images. All of the nanomaterials exhibit superparamagnetic behavior at room temperature. The magnetic properties are due to the core Fe_3O_4 nanoparticles, in addition, the magnetic moments of the RE^{3+} ions are also contributed to the whole magnetization of the Eu^{3+} and Tb^{3+} nanocomposites. Thus, it was observed the efficient magnetic contribution of the Tb^{3+} ion to the magnetization of the Fe_3O_4@SiO_2-(TTA-Tb-AB) and Fe_3O_4@SiO_2-(TTA-Tb-AMB) nanocomposites when compared to the Eu^{3+} counterparts ones.

The photoluminescence data suggest that the T_1 states energies of the TC, AB and AMB ligands are higher than the emitting levels of Eu^{3+} ($^5D_0$) and Tb^{3+} ($^5D_4$), indicating these ligands can transfer energy to the rare earth ions. However, the Fe_3O_4@SiO_2-(TTA-Eu-TTA or AMB) and Fe_3O_4@SiO_2-(TTA-Tb-AB or AMB) nanocomposites present high red and green emissions intensities. These photonic data suggest that the TTA and AMB ligands act as an efficient sensitizers for the red (Eu^{3+}), as well as AB and AMB ligands for the green (Tb^{3+}) emissions in the nanomaterials.

Acknowledgments

The authors are grateful for financial support from the Coordenação de Aperfeiçoamento de Pessoal de Nível Superior (CAPES, Brazil), Conselho Nacional de Desenvolvimento Científico e Tecnológico (CNPq, Brazil), Fundação de Amparo à Pesquisa do Estado de São Paulo (FAPESP, Brazil), Instituto Nacional de Ciência e Tecnologia de Nanotecnologia para Marcadores Integrados (inct-INAMI, Brazil), CNPEM-LNLS synchrotron, Campinas-SP, Brazil under Proposal Nos. SAXS1–14355 (7959), CNPEM-LNNano, Campinas-SP, Brazil under Proposal Nos. TEM-MSC 14828 (7959).

Appendix A. Supplementary data

Supplementary data related to this article can be found at http://dx.doi.org/10.1016/j.jallcom.2016.06.009.

References

[1] L.U. Khan, H.F. Brito, J. Hölsä, K.R. Pirota, D. Muraca, M.C.F.C. Felinto, et al., Red-green emitting and superparamagnetic nanomarkers containing Fe_3O_4

functionalized with calixarene and rare earth complexes, Inorg. Chem. 53 (2014) 12902–12910.
[2] F. Wang, G.M. Pauletti, J. Wang, J. Zhang, R.C. Ewing, Y. Wang, et al., Dual surface-functionalized janus nanocomposites of polystyrene/Fe_3O_4@SiO_2 for simultaneous tumor cell targeting and stimulus-induced drug release, Adv. Mater 25 (2013) 3485–3489.
[3] Z. Fan, M. Shelton, A.K. Singh, D. Senapati, S.A. Khan, P.C. Ray, Multifunctional plasmonic shell-magnetic core nanoparticles for targeted diagnostics, isolation, and photothermal destruction of tumor cells, ACS Nano 6 (2012) 1065–1073.
[4] P.-H. Zhang, J.-T. Cao, Q.-H. Min, J.-J. Zhu, Multi-shell structured fluorescent–magnetic nanoprobe for target cell imaging and on-chip sorting, ACS Appl. Mater. Interfaces 5 (2013) 7417–7424.
[5] S. Comby, E.M. Surender, O. Kotova, L.K. Truman, J.K. Molloy, T. Gunnlaugsson, Lanthanide-functionalized nanoparticles as MRI and luminescent probes for sensing and/or imaging applications, Inorg. Chem. 53 (2014) 1867–1879.
[6] A. Son, A. Dhirapong, D.K. Dosev, I.M. Kennedy, R.H. Weiss, K.R. Hristova, Rapid and quantitative DNA analysis of genetic mutations for polycystic kidney disease (PKD) using magnetic/luminescent nanoparticles, Anal. Bioanal. Chem. 390 (2008) 1829–1835.
[7] H. Sun, X. Zeng, M. Liu, S. Elingarami, G. Li, B. Shen, et al., Synthesis of size-controlled Fe_3O_4@SiO_2 magnetic nanoparticles for nucleic acid analysis, J. Nanosci. Nanotechnol. 12 (2012) 267–273.
[8] D. Shi, M.E. Sadat, A.W. Dunn, D.B. Mast, Photo-fluorescent and magnetic properties of iron oxide nanoparticles for biomedical applications, Nanoscale 7 (2015) 8209–8232.
[9] L.P. Singh, S.K. Srivastava, R. Mishra, R.S. Ningthoujam, Multifunctional hybrid nanomaterials from water dispersible CaF_2:Eu^{3+}, Mn^{2+} and Fe_3O_4 for luminescence and hyperthermia application, J. Phys. Chem. C 118 (2014) 18087–18096.
[10] N. Insin, J.B. Tracy, H. Lee, J.P. Zimmer, R.M. Westervelt, M.G. Bawendi, Incorporation of iron oxide nanoparticles and quantum dots into silica microspheres, ACS Nano 2 (2008) 197–202.
[11] M.J. Li, Z. Chen, V.W.W. Yam, Y. Zu, Multifunctional ruthenium(II) polypyridine complex-based core-shell magnetic silica nanocomposites: magnetism, luminescence, and electrochemiluminescence, ACS Nano 2 (2008) 905–912.
[12] L. Tong, J. Shi, D. Liu, Q. Li, Luminescent and magnetic properties of Fe_3O_4@SiO_2@ Y_2O_3: Eu^{3+} composites with core–shell structure, J. Phys. Chem. C (2012) 7153–7157.
[13] S.-Y. Yu, H.-J. Zhang, J.-B. Yu, C. Wang, L.-N. Sun, W.-D. Shi, Bifunctional magnetic - optical nanocomposites: grafting lanthanide complex onto core-shell magnetic silica nanoarchitecture, Langmuir 23 (2007) 7836–7840.
[14] F. Zhang, G.B. Braun, A. Pallaoro, Y. Zhang, Y. Shi, D. Cui, et al., Mesoporous multifunctional upconversion luminescent and magnetic "nanorattle" materials for targeted chemotherapy, Nano Lett. 12 (2012) 61–67.
[15] J. Zhou, L. Meng, Q. Lu, J. Fu, X. Huang, Superparamagnetic submicromegranates: Fe_3O_4 nanoparticles coated with highly cross-linked organic/inorganic hybrids, Chem. Commun. (2009) 6370–6372.
[16] R. Ghosh Chaudhuri, S. Paria, Core/shell nanoparticles: classes, properties, synthesis mechanisms, characterization, and applications, Chem. Rev. 112 (2012) 2373–2433.
[17] D.L. Leslie-Pelecky, R.D. Rieke, Magnetic properties of nanostructured materials, Chem. Mater 8 (1996) 253–266.
[18] M. Mikhaylova, D.K. Kim, N. Bobrysheva, M. Osmolowsky, V. Semenov, T. Tsakalakos, et al., Superparamagnetism of magnetite nanoparticles: dependence on surface modification, Langmuir 20 (2004) 2472–2477.
[19] O. Moscoso-Londoño, J.S. Gonzalez, D. Muraca, C.E. Hoppe, V.A. Alvarez, A. López-Quintela, et al., Structural and magnetic behavior of ferrogels obtained by freezing thawing of polyvinyl alcohol/poly(acrylic acid) (PAA)-coated iron oxide nanoparticles, Eur. Polym. J. 49 (2013) 279–289.
[20] M. Knobel, W.C. Nunes, L.M. Socolovsky, E. De Biasi, J.M. Vargas, J.C. Denardin, Superparamagnetism and other magnetic features in granular materials: a review on ideal and real systems, J. Nanosci. Nanotechnol. 8 (2008) 2836–2857.
[21] A.L. Morel, S.I. Nikitenko, K. Gionnet, A. Wattiaux, J. Lai-Kee-Him, C. Labrugere, et al., Sonochemical approach to the synthesis of Fe_3O_4@SiO_2 core-shell nanoparticles with tunable properties, ACS Nano 2 (2008) 847–856.
[22] S. Laurent, D. Forge, M. Port, A. Roch, C. Robic, L. Vander Elst, et al., Magnetic iron oxide nanoparticles: synthesis, stabilization, vectorization, physicochemical characterizations, and biological applications, Chem. Rev. 108 (2008) 2064–2110.
[23] F. Fajaroh, H. Setyawan, A. Nur, I.W. Lenggoro, Thermal stability of silica-coated magnetite nanoparticles prepared by an electrochemical method, Adv. Powder Technol. 24 (2013) 507–511.
[24] M. Liong, J. Lu, M. Kovochich, T. Xia, S.G. Ruehm, A.E. Nel, et al., Multifunctional inorganic nanoparticles for imaging, targeting, and drug delivery, ACS Nano 2 (2008) 889–896.
[25] K. Binnemans, Lanthanide-based luminescent hybrid materials, Chem. Rev. 109 (2009) 4283–4374.
[26] J.-C.G. Bünzli, S.V. Eliseeva, Intriguing aspects of lanthanide luminescence, Chem. Sci. 4 (2013) 1939–1949.
[27] H.F. Brito, O.L. Malta, M.C.F.C. Felinto, E.E.S. Teotonio, Luminescence phenomena involving metal enolates, in: J. Zabicky (Ed.), The Chemistry of Metal Enolates Part 1, John Wiley Sons Ltd., England, 2009, pp. 131–184.
[28] G.F. de Sá, O.L. Malta, C. de Mello Donegá, a. M. Simas, R.L. Longo, P. a Santa-Cruz, et al., Spectroscopic properties and design of highly luminescent lanthanide coordination complexes, Coord. Chem. Rev. 196 (2000) 165–195.
[29] J.-C.G. Bünzli, On the design of highly luminescent lanthanide complexes, Coord. Chem. Rev. 293–294 (2015) 19–47.
[30] J.C.G. Bünzli, Lanthanide luminescence for biomedical analyses and imaging, Chem. Rev. 110 (2010) 2729–2755.
[31] S. Cotton, Electronic and magnetic properties of the lanthanides, in: S. Cotton (Ed.), Lanthanide and Actinide Chemistry, John Wiley Sons Ltd., England, 2005, pp. 61–83.
[32] W. Stöber, A. Fink, E. Bohn, Controlled growth of monodisperse silica spheres in the micron size range, J. Colloid Interface Sci. 26 (1968) 62–69.
[33] Y. Yong, Y. Bai, Y.F. Li, L. Lin, Y. Cui, C. Xia, Preparation and application of polymer-grafted magnetic nanoparticles for lipase immobilization, J. Magn. Magn. Mater 320 (2008) 2350–2355.
[34] S. Sayin, M. Yilmaz, Synthesis of a new calixarene derivative and its immobilization onto magnetic nanoparticle surfaces for excellent extractants toward Cr(VI), As(V), and U(VI), J. Chem. Eng. Data 56 (2011) 2020–2029.
[35] A.V. Teixeira, I. Morfin, F. Ehrburger-Dolle, C. Rochas, P. Panine, P. Licinio, et al., Structure and magnetic properties of dilute ferrofluids suspended in gels, Compos. Sci. Technol. 63 (2003) 1105–1111.
[36] C. Meiorin, O.M. Londoño, D. Muraca, L.M. Socolovsky, K.R. Pirota, M.I. Aranguren, et al., Magnetism and structure of nanocomposites made from magnetite and vegetable oil based polymeric matrices, Mater. Chem. Phys. 175 (2016) 81–91.
[37] S.-H. Chen, J. Teixeira, Structure and fractal dimension of protein-detergent complexes, Phys. Rev. Lett. 57 (1986) 2583–2586.
[38] SASfit: Small Angle Scattering (SAS) Data Analysis Software for Fitting Simple Form Factors and Structure Factors https://kur.web.psi.ch/sans1/SANSSoft/sasfit.html (accessed 28.06.15).
[39] A. Guinier, G. Fournet, Small-angle Scattering of X-rays, John Wiley & Sons, Inc., New York, 1955.
[40] E.V. Shtykova, X. Huang, N. Remmes, D. Baxter, B. Stein, B. Dragnea, et al., Structure and properties of iron oxide nanoparticles encapsulated by phospholipids with poly(ethylene glycol) tails, J. Phys. Chem. C 111 (2007) 18078–18086.
[41] Y.-C. Lin, C.-Y. Chen, H.-L. Chen, T. Hashimoto, S.-A. Chen, Y.-C. Li, Hierarchical self-assembly of nanoparticles in polymer matrix and the nature of the interparticle interaction, J. Chem. Phys. 142 (2015) 214905-1–214905-14.
[42] G. Marcelo, F. Catalina, I. Bruvera, C. Marquina, G. Goya, Specific power absorption of silica-coated magnetite cubes, Curr. Nanosci. 10 (2014) 676–683.
[43] K. Binnemans, Interpretation of europium(III) spectra, Coord. Chem. Rev. 295 (2015) 1–45.
[44] L.D. Carlos, Y. Messaddeq, H.F. Brito, R.A. Sá Ferreira, V. De Zea Bermudez, S.J.L. Ribeiro, Full-color phosphors from europium(III)-based organosilicates, Adv. Mater 12 (2000) 594–598.
[45] E. Rezende Souza, I.G.N. Silva, E.E.S. Teotonio, M.C.F.C. Felinto, H.F. Brito, Optical properties of red, green and blue emitting rare earth benzenetricarboxylate compounds, J. Lumin 130 (2010) 283–291.
[46] A.V.S. Lourenço, C.A. Kodaira, E.M. Ramos-Sanchez, M.C.F.C. Felinto, H. Goto, M. Gidlund, et al., Luminescent material based on the [$Eu(TTA)_3(H_2O)_2$] complex incorporated into modified silica particles for biological applications, J. Inorg. Biochem. 123 (2013) 11–17.
[47] O.L. Malta, L.D. Carlos, Intensities of 4f-4f transitions in glass materials, Quim. Nova 26 (2003) 889–895.
[48] R.A. Sá Ferreira, S.S. Nobre, C.M. Granadeiro, H.I.S. Nogueira, L.D. Carlos, O.L. Malta, A theoretical interpretation of the abnormal $^5D_0 \rightarrow {}^7F_4$ intensity based on the Eu^{3+} local coordination in the $Na_9[EuW_{10}O_{36}]\cdot 14H_2O$ polyoxometalate, J. Lumin 121 (2006) 561–567.
[49] A.S. Borges, J.D.L. Dutra, R.O. Freire, R.T. Moura, J.G. Da Silva, O.L. Malta, et al., Synthesis and characterization of the Europium(III) pentakis(picrate) complexes with imidazolium countercations: structural and photoluminescence study, Inorg. Chem. 51 (2012) 12867–12878.
[50] J. Kai, M.C.F.C. Felinto, L. a. O. Nunes, O.L. Malta, H.F. Brito, Intermolecular energy transfer and photostability of luminescence-tuneable multicolour PMMA films doped with lanthanide–β-diketonate complexes, J. Mater. Chem. 21 (2011) 3796–3802.
[51] P.A. Santa-Cruz, F.S. Teles, SpectraLux Software v.1.0, 2003. Ponto Quântico Nanodispositivos, RENAMI.